Optical Position Measurement for a Large Gap Magnetic Suspension System

Design and Performance Analysis

Sharon S. Welch, James I. Clemmons, Jr., Kevin J. Shelton, and Walter C. Duncan

Optical Position Measurement for a Large Gap Magnetic Suspension System

Design and Performance Analysis

Sharon S. Welch
Langley Research Center • Hampton, Virginia

James I. Clemmons, Jr.
ViGYAN, Inc. • Hampton, Virginia

Kevin J. Shelton and Walter C. Duncan
Lockheed Engineering & Sciences Company • Hampton, Virginia

Introduction

The first large gap magnetic suspension systems were developed more than 30 years ago as wind tunnel magnetic suspension and balance systems (MSBS). (See ref. 1.) More recently, large gap magnetic suspension systems have been developed for vibration isolation and pointing applications. Differences in coil geometries and positioning requirements for the vibration isolation application have led to new approaches for sensing and controlling the position and attitude of the suspended element. In this paper, the design and performance of an optical position measurement system (OMS) are analyzed. The OMS was developed for a six-degree-of-freedom, large gap magnetic suspension system (LGMSS) (ref. 2) for vibration isolation and pointing.

The LGMSS features several large electromagnets in a planar configuration that suspend a cylindrical element containing a permanent magnet core (fig. 1). The element is suspended 91 cm (36 in.) above the magnets. To stabilize suspension and control motion in six degrees of freedom, information on the position and on the attitude of the suspended element is required. An optical sensing system based on linear charge-coupled device (CCD) sensors has been designed to determine the position and attitude of the suspended element in six degrees of freedom and to supply this information to the LGMSS control system. In the OMS, multiple one-dimensional imaging sensors are used to detect small infrared light-emitting diode (LED) targets embedded in the surface of the suspended element. The position and attitude of the element are determined from the measured locations of the images in the sensors and from transformation equations that relate the coordinates of the target images in the reference frames of the sensors to the position and orientation of the suspended element in the laboratory reference frame. Rigid body motion has been assumed.

The position and orientation of the suspended element are defined by the alignment of a body fixed coordinate system defined by x_b, y_b, and z_b with respect to a laboratory fixed coordinate system defined by x_f, y_f, and z_f. (See fig. 1.) Both coordinate systems are right-hand Cartesian. The position of the element is defined by the x, y, and z location of the origin of the body frame in the laboratory frame of reference (denoted x_{cm}, y_{cm}, and z_{cm}) and the orientation of the body frame with respect to the laboratory frame defined by the Euler angles of yaw, pitch, and roll and the rotation sequence depicted in figure 2. The magnetic suspension system must position the element to x_f, y_f, and $z_f = \pm 0.0254$ cm (± 0.01 in.) of the initial 0-in. alignment and to ψ, θ,

and $\phi = \pm 0.02°$. The LGMSS must meet these specifications for a range of element sizes and weights. In particular, suspension to this accuracy is to be demonstrated for two sizes of cylindrical elements: 35.56 cm (14 in.) long by 5.08 cm (2.0 in.) in diameter and 35.56 cm long by 10.16 cm (4.0 in.) in diameter. (See fig. 3.) In addition, the LGMSS must respond to yaw commands of $1.0°$ over $360°$ within a 10-sec interval allowed for repositioning and settling. No commands can be input for pitch and roll; rather, they are constrained to $0°$.

The LGMSS has a digital controller. Both the accuracy of the position estimate and the rate at which position and attitude information is made available to the controller influence the positioning accuracy of the magnetic suspension system. An accuracy requirement of 30 percent of the total error budget for the LGMSS was established for the position measurement system. That is, the position sensing system should track the element from $\psi = 0°$ to $360°$ with an accuracy (i.e., 1 standard deviation) for x_{cm}, y_{cm}, and z_{cm} of ± 0.00762 cm (± 0.003 in.) and for ψ, θ, and ϕ of $\pm 0.006°$.

The rate at which the sensing system must update the estimates of position and attitude for the controller to stabilize suspension of the suspended element is a function of the natural frequencies of the magnetic suspension system. The natural frequencies are functions of the configuration of the coil, size and mass distribution of the element and core, and orientation of the core magnetization vector. Initially, the LGMSS was set at 20 samples per second. At the time this sample rate was set, the number of coils, the exact coil configuration, the size of the suspended element, and the permanent magnet core sizes for the LGMSS were unknown. Therefore, the final system configuration as designed operates at a rate of 40 samples per second with either a small or large cylindrical element that contains a small or a large permanent magnet core, respectively, which has been magnetized in the vertical direction. (See fig. 3.)

Symbols and Abbreviations

b, f	coordinate systems of body and laboratory fixed reference frame, respectively (fig. 1)
F	error in position of suspended element
$I(n)$	intensity (fig. 14)
k	time index

k_{ij}, m_{ij}	elements of rotation matrices for x and y cameras, respectively
N_x, N_y	window width in pixels of x and cameras, respectively
$\mathbf{r}_b$	position vector for point target in body reference frame
$\mathbf{r}_{cm}$	position vector of center of body reference frame in laboratory reference frame
$\mathbf{r}_f$	position vector for point target in laboratory reference frame
$\mathbf{R}$	position and attitude vector of suspended element
$\mathbf{T}$	transformation matrix for rigid body (Euler) rotation
W	matrix of weights for target positions
W_j	weight for jth target position
W_x, W_y	weight for centroid estimate in x and y cameras, respectively
$x(i,j)$, $y(i,j)$	centroid location in ith x (or y) sensor of target j
x^c, y^c, z^c	camera position in laboratory reference frame
x_b, y_b, z_b	coordinates of a point target in body reference frame
x_{cm}, y_{cm}, z_{cm}	coordinates of origin of body reference frame in laboratory reference frame
x_f, y_f, z_f	coordinates of a point target in laboratory reference frame
$\bar{x}$	centroid of light distribution (fig. 14)
$\mathbf{\Delta}$	vector of delta changes in position and attitude of suspended element
θ	pitch angle of element, deg
σ	standard deviation
$\bar{\sigma}$	calculation of second moment of light distribution (fig. 14)
ϕ	roll angle of element, deg
ϕP, ϕT	CCD clock signals (fig. 17)
ψ	yaw angle of element, deg

Abbreviations:

CCD	charge-coupled device
DSP	digital signal processor
LED	light-emitting diode
LGMSS	large-gap magnetic suspension system
OMS	optical position measurement system
TTL	transistor-transistor logic
SNR	$= \dfrac{\text{Peak signal}}{\text{Standard deviation of background noise}}$

Design of Optical Measurement System

Sensors

The initial design and development of specifications for the LGMSS began in 1986. Simultaneously, a feasibility study of the LGMSS was initiated (ref. 3) and a survey of commercially available position measurement systems was conducted. The survey results showed that no commercially available position measurement system could meet all the requirements for the LGMSS and that a measurement system would have to be developed to meet these requirements. Also, optical sensing was determined as best for position measurement in the LGMSS because of its potential for high-resolution, high-speed, and nonintrusive measurements. Laser-based interferometric and CCD-based optical sensing systems were found to have the greatest reliability, speed, and measurement accuracy. Of these two types, the CCD-based sensing systems were known to be relatively impervious to magnetic fields. At the time of the survey, a CCD-based position measurement system was already in use in a large gap magnetic suspension system, the 13-Inch Magnetic Suspension and Balance System (MSBS) wind tunnel at the Langley Research Center. (See ref. 4.) Preliminary findings from the Langley MSBS experiments showed that a CCD-based system would provide more reliable and accurate measurements in the LGMSS environment than would a laser-based interferometric system.

Two CCD sensor geometries were evaluated for use in the LGMSS application: linear CCD arrays in which small discrete photosensitive elements are arranged in a single line and planar CCD arrays in which the photosensitive elements are arranged in a grid. The state of the art in processing and position estimation was assessed and a close-range photogrammetric approach was selected for tracking the location of the suspended element. In this approach, multiple cameras are used in conjunction

with multiple-point targets and triangulation to determine the locations of the targets in an external frame of reference. This selection was based upon the fact that more sophisticated algorithms which relied upon full images of the suspended element or pattern matching were too computationally intensive, given the capability of processors at that time, to meet the rate requirement of 20 samples per second. Therefore, the CCD sensor geometries were evaluated based on the number of cameras required to meet the accuracy requirements for point tracking, and the speed or time required to acquire data from the array and to track the different targets.

To estimate the number and spatial resolution of cameras required to meet the LGMSS accuracy specifications, a photogrammetric sensing system was simulated using the simultaneous triangulation and resection system (STARS) computer program. (See ref. 5.) Cameras were located above the suspended element and angled as close to 45° as possible with respect to the vertical. (The errors in the estimates of x_f, y_f, and z_f are a minimum for a 45° pointing angle. See ref. 6.) For a fixed camera resolution and a fixed uncertainty in the camera locations in the external frame of reference, the accuracy of detecting a point target within the field of view improves approximately as the square root of the number of cameras. Assuming that the location of a target image could be resolved to 0.1 pixel in a camera, 6 two-dimensional CCD array cameras with 1024 by 1024 pixels would be required to yield a 1σ uncertainty in the position of a point target in the laboratory reference frame of 0.001016 cm (0.0004 in.) in x_f and y_f and 0.001524 cm (0.0006 in.) in z_f.

At the time of the evaluation, the state of the art for planar CCD arrays was a device with 512 by 512 pixels. Thus, more than 20 two-dimensional CCD cameras would be needed to achieve the same accuracy in point tracking as was predicted for a camera with 1024 by 1024 pixels. However, state-of-the-art linear arrays featured 4096 pixels. Based on the assumption that two linear CCD arrays oriented orthogonally would have a resolution equivalent to a two-dimensional array, only four linear CCD cameras with 4096 pixels would be needed. (This assumption, in hindsight, was a poor one. System calibration of linear CCD arrays is more difficult and the uncertainties in the camera parameters can be larger than were modeled in the STARS simulation.)

At least three targets are required to solve the transformation equations. Then, by assuming equal uncertainty in the locations of targets and equal moment arms, the analyst can improve the estimates of position and attitude roughly as the square root of the number of targets. Thus, for a 1σ uncertainty in a target position of 0.001016 cm in x_f and y_f and of 0.001524 cm in z_f, at least six targets are needed to meet the yaw and pitch accuracy requirements. (To meet the accuracy requirement for roll for the smaller element, more than 10 targets are required, assuming the same 1σ uncertainty in target position.)

In the case of the two-dimensional array, all the targets could be imaged simultaneously and, therefore, the only consideration was whether the image data could be digitized and stored fast enough to allow time for processing. However, the linear array would require the targets to be multiplexed in time for target identification. Therefore, the total time would be the product of the number of targets and the time to acquire a single target. In CCD arrays, the signals generated by each photosensitive element (or pixel) are read out in a serial fashion. As a result, for a fixed data rate, the greater the number of pixels in the array, the greater the read-out time. The maximum data rate for CCD arrays at the time of the evaluation was about 20 MHz. This data rate corresponded to the conversion rates for the fastest analog-to-digital converters (ADC's) (above 8-bit resolution). At these rates, an array with 512 by 512 pixels required at least 13 msec to be read out. The time required to read out a linear array of 4096 pixels at 20 MHz was 205 μsec. Therefore, assuming an integration time of about 2 msec, the time to image and store the data from six targets was about 15 msec for the two-dimensional array and 13 msec for the linear array.

The choice of CCD array geometry was ultimately based on the greater one-dimensional spatial resolution of linear CCD arrays and the fact that the design of the electronics for data storage and processing was much simpler for the linear array. Thus, a linear CCD array with 2048 pixels was selected as the basic sensor element for the optical measurement system (OMS). This CCD array had the maximum pixel density for linear CCD arrays at that time. The system was designed for 16 cameras with 8 targets embedded in the surface of the suspended element. This design ensured that at least 6 targets could each be resolved to 0.1 pixel in at least 12 cameras for the full range of motion of the suspended element.

Targets

The decision was made early in the OMS design phase to use light-emitting diodes (LED's) as active targets rather than passive reflective targets. Passive targets do not require electronics or power on the suspended element; however, they must be large to return a strong signal. Passive targets require a

powerful source of illumination; also, when a linear CCD detector is used, one passive target is not readily distinguishable from another. Further, the large target centroid location is more difficult to determine from oblique camera angles.

Developing active targets for the OMS proved challenging for several reasons. If the targets were to be detected from different camera perspectives, then the light from the targets would have to radiate in a nearly hemispherical pattern. This approach would require high light output from the LED's to obtain a high camera signal-to-noise ratio (SNR) for a short integration period (less than 3 msec). To obtain that high a light output, the LED's would have to be driven at the maximum allowable current levels. High current levels tended to overheat the LED's; also, because the LED's were to be powered with batteries, the run time decreased.

Figure 4 shows a schematic diagram and photographs of the LED targets developed for the OMS. A single LED chip that measures 0.05 cm (0.02 in.) across the diagonal is soldered into a reflector with an outside diameter measuring 0.11938 cm (0.047 in.). The base of the reflector shown in figure 4 is a heat sink. Initial tests indicated that the heat sink was required to prevent destruction of the LED when it was operating at the high current pulses used in this application because early tests had disclosed that nearly 50 percent of the light was attenuated by a diffuser. During tracking, the LED's are pulsed on for 2.083 msec at 200 mA. The LED's are top emitting with a wavelength of 880 nm. Furthermore, no lens or defuser is used on the LED. Figure 5 shows the target geometry and a plot of the normalized target light output as a function of angle.

The LED's are multiplexed in time for target identification. Power and driver electronics for the LED's are located inside the cylinder. (See fig. 6.) Two rechargeable batteries are used to power the targets and electronics. The batteries are rated for 250 mA-hours of operation. Tests on a single battery showed that battery lifetime will depend upon the method of charge and discharge. Curves of output voltage over time are shown in figure 7 for different discharge rates.

Processors

The design of the processor evolved over a 5-year period. This evolution was driven by the requirements for high speed and high accuracy. Maximum accuracy and speed required that the centroid estimate be calculated using floating point arithmetic. The total time to transfer the data from the cam-

eras to a single central processor, to execute the centroid algorithm 16 times in sequence, and to solve the transformation equations exceeded 50 msec. As a result, a decision was made to design an ADC board and a digital signal processor (DSP) board for each camera. The digitized data from a camera would be stored and the centroid of the one-dimensional target image would be calculated on the DSP board. The 16 centroids would be transferred to a central processor where the x, y, and z positions of the targets and the position and attitude of the suspended element would be calculated.

In 1987, standard DSP's and microprocessors did not have built-in floating point capability. Thus, additional floating point processors were originally included in the design of the camera processors. Advancements in technology, which occurred around 1988, led to the use of high-speed DSP's with built-in floating point capability.

The design of the central processor evolved as well. Originally, the calculations of the target positions and the position and attitude of the suspended element were to be performed in a high-speed array processor that was external to the OMS. However, communications between the OMS and external processor proved too slow. The basic processor was fast enough to perform the computations in the required time, but the data transfer times between the sensor DSP's and the external processor were too great to meet the 20-sample-per-second requirement. As a result, DSP 17 (MATH DSP) was added to the OMS backplane and used to calculate the target positions and the position and attitude of the suspended element.

The software for the processor is structured so that data acquisition and computations are done both in parallel as well as pipelined. A diagram illustrating the structure of the software is shown in figure 8. Each frame is divided into 12 intervals, the intervals being equal to the camera integration periods. During interval 1, the first target is pulsed on and imaged in parallel in the 16 cameras. During interval 2, the data are digitized, stored in random access memory (RAM) on each camera DSP board, and the calculations of the centroids are begun in the camera DSP's as the second target is pulsed on and imaged. At the end of interval 2, the centroids are transferred to the MATH DSP. During interval 3, the third target is imaged, the centroids of the second target are calculated in the camera DSP's, and the x, y, and z position of the first target is calculated in the MATH DSP. Intervals 4–8 are identical to interval 3. During intervals 9–12, the targets are not illuminated. The calculations of the centroids and

4

the x, y, and z position estimates of the eighth target are calculated during intervals 9 and 10, respectively. During the last two intervals, the position and attitude of the suspended element are calculated.

Optical Measurement System

The OMS consists of eight sensing units stationed symmetrically about the center of the suspension magnets and 8 ft above the top of the magnets. (See fig. 9.) Each sensing unit has two linear charge-coupled device (CCD) cameras, denoted x and y, oriented in orthogonal directions. (See fig. 10.) The sensing units are attached to a support structure that is constructed of wood and fiberglass beams with aluminum mounts. The mounts allow each sensing unit to be oriented in two independent angular directions. The distance between each sensing unit and the origin of the laboratory reference frame is approximately 183 cm (72 in.).

Camera components include a Thompson-CSF linear CCD array sensor with 2048 photosensitive elements, a 5.08- by 5.08-cm single-element cylindrical lens, an infrared filter, driver electronics for the CCD array, and thermoelectric cooler and control circuitry. The cooler and control circuitry is required to keep electronic components on the CCD driver board from overheating at the clock speeds used in this application.

The cylindrical lens images the light emitted by an LED target as a one-dimensional (line) image on the CCD array. Charges are generated in each photodiode element in response to light striking the array and they accumulate during the sensor integration time. Following the integration time, the accumulated charge is read out as an analog video signal. That is, the voltage signal is output for each photodiode element which is proportional to the integrated light intensity falling on that element (pixel). The sensor field of view is approximately 60 by 60 cm. Thus, an LED target covers roughly 0.002 of the total field of view. The width of the lens point spread function (PSF) is about the width of an individual pixel and both contribute to blurring of the target image. The target is small relative to the total field of view so the image of a target diode when located in the center of the field of view appears as a nearly Gaussian distribution of light along the array. (See fig. 11.)

The CCD array is not equally sensitive to all wavelengths of light; rather, it has a peak sensitivity in the infrared around 775 nm. To improve the SNR, an infrared filter is mounted in front of the lens to limit the background light reaching the sensor. The cutoff for the filter is 830 nm.

An infrared laser is located on the camera support structure directly above the suspended element. The laser is used to time the flashing of the LED targets. A small phototransistor, approximately 0.127 cm (0.050 in.) in diameter, is embedded in the center of the top surface of the cylindrical element. The target LED's are turned on and off in response to the illumination of this phototransistor. The flashing of the timing laser is controlled through the optical sensing system controller. A timing diagram is shown in figure 12.

A 20 megasample per second, 10-bit, ADC digitizes the signal from a camera and stores the digital values in RAM located on the camera DSP board. The centroid of the one-dimensional digital image is computed using a Texas Instruments TMS320C30 DSP. In addition, an SNR is determined for each measurement. The SNR provides information to determine weighting factors, which are carried along with the position information. In the MATH DSP, the position information is multiplied by the weighting factors to determine an estimate of the position and attitude. As the SNR for any given measurement approaches 0, the less the measurement contributes to the position and attitude estimate. Each x and y centroid estimate and weighting factor is stored as a 32-bit floating point number.

Figure 13 shows a block diagram of signal flow and processing for the OMS. The function of each component shown in the diagram of figure 13 is as follows. A DSP is used for each camera to control the camera background adjustment, integration time, and signal readout. The DSP's are also used to perform calculations such as computing the centroid of each image formed by an LED target, the SNR of the signal, and the background level, as well as to perform an estimate of the total error for the corresponding centroid estimate. The MATH DSP is used to calculate the matrix elements, execute the time interpolation algorithm, and perform the tracking algorithm to determine the six position and attitude estimates. A 16-bit microprocessor is used to control the flow of instructions from the DSP's to and from a personal computer and to control communication with the LGMSS controller. The personal computer is used to send instructions to the optical sensing system and to display system status information.

Calculating Position and Attitude

The x and y locations of the projected images of each of the 8 target LED's in each of the 16 cameras are determined by calculating the location of the centroid of the one-dimensional image (or light

distribution) along the respective x and y CCD arrays. The six parameters, x_{cm}, y_{cm}, z_{cm}, ψ, θ, and ϕ, which give the position and attitude of the suspended element at one point in time, are determined by solving two sets of linear equations: the first relates the measured x and y locations of the target LED images in the 16 cameras to the x_f, y_f, and z_f coordinates of each target LED; the second relates a change in the x_f, y_f, and z_f coordinates of all eight target LED's to a change in the six (position and attitude) parameters. To correct for element motion between the image acquisitions of each target LED, a Lagrangian time interpolation algorithm is used. The interpolation is performed over the x_f, y_f, and z_f coordinates of each target using the current estimates and the estimates from the three previous frames. The coordinates of each target are predicted at the beginning of the current frame. The interpolated x_f, y_f, and z_f of the target LED's are used to predict the position and attitude of the suspended element.

Centroiding Algorithm

A flowchart of the centroiding algorithm is shown in figure 14 in which three searches are conducted for the peak pixel location. First, a coarse search of every third pixel is made for the peak pixel location. (A search of every pixel would take too long.) A coarse search for the peak is performed each time because targets will move in and out of the sensor field of view as the position and attitude of the element changes. Searching the entire array for the peak requires less software than tracking the centroid estimates and determining when a target has departed or entered the field of view. If the peak location is determined to be within 50 pixels of either edge of the array, then an error flag is set and the centroid is not computed.

Second, if the peak lies within the central region of the array, then a search of every pixel is made for the peak location ±10 pixels on either side of the initial peak location. This new peak location is stored and used as a pointer into the array.

Each pixel has a slightly different gain and zero point. Before the centroid is computed, the values of light intensity are corrected for pixel nonuniform responsivity and the background light level is subtracted for the 81 pixels centered about the peak.

Third, a search for the peak location is performed over the corrected light intensity values. This "true" peak location then replaces the old pointer.

When the peak location is established, the width of the target image distribution is determined by calculating the second moment of the distribution. The width of the distribution is determined because the amplitude of the target image will change as the target moves within the camera field of view. (See fig. 15.) As discussed in reference 7, when the signal amplitude and shape vary, a centroid calculated over a window that is a fixed size will cause a significant error either due to truncation of the signal when the image distribution is large relative to the window width or to noise when the image width is narrow relative to the window width. To increase the dynamic range of the imaging system, the second moment of the distribution is calculated before the centroid and an optimal window; that is, a window is determined that is matched in width to the target image distribution. The x and y centroid locations are subsequently determined by

$$x(i,j) = \frac{\sum\limits_{n=\text{Peak}-\frac{N_x}{2}}^{n=\text{Peak}+\frac{N_x}{2}} n I_{i,j}(n)}{\sum\limits_{n=\text{Peak}-\frac{N_x}{2}}^{n=\text{Peak}+\frac{N_x}{2}} I_{i,j}(n)} \qquad (1a)$$

$$y(i,j) = \frac{\sum\limits_{m=\text{Peak}-\frac{N_y}{2}}^{m=\text{Peak}+\frac{N_y}{2}} m I_{i,j}(m)}{\sum\limits_{m=\text{Peak}-\frac{N_y}{2}}^{m=\text{Peak}+\frac{N_y}{2}} I_{i,j}(m)} \qquad (1b)$$

where i denotes the particular sensing unit; j denotes the target; n and m are the pixel numbers in the x and y cameras, respectively; $I(n)$ and $I(m)$ are the digital values of the light intensity for pixels n and m; peak is the pixel location of peak signal; and N_x and N_y are the half-widths of the window in the x and y camera, respectively.

Tracking Algorithm

The position and attitude of the suspended element are defined by the parameters x_{cm}, y_{cm}, z_{cm}, ψ, θ, and ϕ. The position vector $\mathbf{r}_{bj}$ of diode j in the body frame with coordinates x_{bj}, y_{bj}, and z_{bj} is related to the position vector $\mathbf{r}_{fj}$ of diode j in the fixed frame with coordinates x_{fj}, y_{fj}, and z_{fj} by

$$\mathbf{r}_{fj} = \mathbf{r}_{cm} + \mathbf{T}\mathbf{r}_{bj} \qquad (2)$$

where $\mathbf{T}$, the rotation matrix, is

$$\mathbf{T} = \begin{bmatrix} \cos(\theta)\cos(\psi) & -\cos(\phi)\sin(\psi) + \sin(\phi)\sin(\theta)\cos(\psi) & \sin(\phi)\sin(\psi) + \cos(\phi)\sin(\theta)\cos(\psi) \\ \cos(\theta)\sin(\psi) & \cos(\phi)\cos(\psi) + \sin(\phi)\sin(\theta)\sin(\psi) & -\sin(\phi)\cos(\psi) + \cos(\phi)\sin(\theta)\sin(\psi) \\ -\sin(\theta) & \sin(\phi)\cos(\theta) & \cos(\phi)\cos(\theta) \end{bmatrix}$$

Similarly, the x_{ij} and y_{ij} coordinates of diode j in the frame of sensing unit i are related to the coordinates of diode j in the laboratory reference frame by the colinearity equations (ref. 8)

$$x_{ij} - x_p = f_x \left[\frac{m_{11}(x_{fj} - x_{ix}^C) + m_{12}(y_{fj} - y_{ix}^C) + m_{13}(z_{fj} - z_{ix}^C)}{m_{21}(x_{fj} - x_{ix}^C) + m_{22}(y_{fj} - y_{ix}^C) + m_{23}(z_{fj} - z_{ix}^C)} \right]$$
(3a)

$$y_{ij} - y_p = f_y \left[\frac{k_{11}(x_{fj} - x_{iy}^C) + k_{12}(y_{fj} - y_{iy}^C) + k_{13}(z_{fj} - z_{iy}^C)}{k_{21}(x_{fj} - x_{iy}^C) + k_{22}(y_{fj} - y_{iy}^C) + k_{23}(z_{fj} - z_{iy}^C)} \right]$$
(3b)

where x_{ix}^C, y_{ix}^C, and z_{ix}^C are the x, y, and z positions of the perspective center of camera x (or camera y for subscript y) in the fixed frame; f_x and f_y are the focal lengths of the lenses in cameras x and y, respectively; x_{pi} and y_{pi} are the principal points of the ith x and y cameras; and m_{ij} and k_{ij} are elements of the rotation matrices for each camera and are functions of the camera pointing angles. The equations are functions of the locations of the ith camera in the fixed frame, the focal lengths of the cameras, and the fixed-frame coordinates of the jth LED target.

From equations (3a) and (3b), the x_f, y_f, and z_f locations of each target are determined using the method of weighted least squares. Lagrangian interpolation is performed on the current estimates of x_f, y_f, and z_f and the three previous time estimates to yield a prediction of the locations of each target at the beginning of the sample interval. The interpolated x_f, y_f, and z_f locations of the eight targets are used to estimate position and attitude.

The position and attitude of the suspended element are determined by solving for the transformation from the body reference frame to the laboratory reference frame, where rigid body motion is assumed. The equations are solved using a Gauss-Newton method. The solution for sample time k corresponding to the beginning of the kth frame of data is the solution to

$$\min_{\boldsymbol{\Delta}_k \varepsilon \mathbf{R}^n} \frac{1}{2} \| W_k (\delta F_k \boldsymbol{\Delta}_k + F_k) \|_2^2$$
(4)

where

$$F_k = (\mathbf{r}_f - \mathbf{r}_{cm} - \mathbf{T}\mathbf{r}_b)_k$$

and δF_k denotes the Jacobian of F_k and W_k is the weighting matrix composed of eight weighting terms $(Wj)_k$, one for each target position estimate. The solution to equation (4) is obtained using Householder QR factorization. (See ref. 9.) The position and attitude for sample time k are then determined by

$$\mathbf{R}_k = \mathbf{R}_{k-1} + \boldsymbol{\Delta}_k$$

where $\mathbf{R}$ is a vector with components x_{cm}, y_{cm}, z_{cm}, ψ, θ, ϕ, and the position and attitude of the model at k or $k-1$; and $\boldsymbol{\Delta}$ is the solution to equation (4) at k.

Weighting Factors

Weighting factors are determined for each x and y centroid estimate as well as for each target position estimate x_f, y_f, and z_f. Weighting the measurements can improve the estimate of target position when the weights are inversely related to the error in the measurement. Also, weighting the measurement provides a simple means of eliminating bad data (e.g., target not in the field of view, signal too low, etc.) When the calculated weight falls below a preset threshold, the weight is set to 0 and the measurement does not contribute to the estimates of position and attitude.

The calculated weighting factors for the centroid estimates are the inverse of the total predicted error multiplied by a constant. That is,

$$W_x(i,j) = \frac{C}{\varepsilon_x(i,j)}$$
(5a)

$$W_y(i,j) = \frac{C}{\varepsilon_y(i,j)}$$
(5b)

where $W_x(i,j)$ and $W_y(i,j)$ denote the weighting factors; $\varepsilon_x(i,j)$ and $\varepsilon_y(i,j)$ denote the predicted error for the ith x or y sensor of the jth target; and C denotes the constant. The predicted error $\varepsilon_x(i,j)$ or $\varepsilon_y(i,j)$ is calculated as the sum of three terms: the first term is dependent upon the SNR, the second term is the residual error after the cameras were

calibrated to determine the optical distortion, and the third term is a function of the proximity of the current target image to the target images acquired during the previous integration periods of the current frame. The third error term, the proximity term, is calculated to account for any error from the residual charge on the CCD sensor. The dependence of the error on SNR, residual charge, and residual errors after camera calibrations is described in the section, "Performance Analysis."

When weighting factors are determined for each centroid estimate, they can be determined for each target position estimate at k. These weighting factors are the same for x_f, y_f, and z_f for a given target and sample time and are calculated from the centroid weighting factors as

$$W_j = \frac{1}{16} \sum_{i=1}^{8} [W_x(i,j) + W_y(i,j)] \qquad (6)$$

Calibration Techniques

Calibrations are performed to correct for errors and determine the (unknown) locations of each camera in the laboratory reference frame. Two principal calibrations are necessary—calibration of each camera and calibration of the overall sensing system. Each camera is calibrated to determine both the response of the CCD sensor to the location of light along the array and the correction for optical distortion. Calibration of the overall system is performed to determine the exterior orientation parameters of the cameras; that is, the locations and pointing angles of the cameras with respect to the laboratory reference frame.

Camera Calibrations

Variations in the predicted location of the centroid as a function of position along the CCD array will result due to nonuniformities in pixel sensitivity in the detector and optical distortions in the projected target image. Calibrations are performed to correct for these errors. To determine the pixel responsivity for a CCD array, a (nearly) spatially uniform direct current (dc) light source is positioned over the end of a camera with the lens in place. The average output at each pixel is obtained for nine integration times ranging from 1 to 9 msec. The average output at each integration time is computed for 100 scans at that setting. A line is fitted to the output of each pixel as a function of integration time. The slope of the line and the Y intercept are calculated for each pixel as the averages from 30 trials.

The slope corresponds to the responsivity and the Y intercept corresponds to the voltage output for no light on the sensor. The response of each pixel is normalized to the peak response along the CCD array. The inverse of the normalized number for each pixel and the Y intercept are stored in look-up tables and used to correct subsequent scans. Representative graphs of sensor nonuniform responsivity correction and offset are in figure 16, which shows two distinct lines. The distinct lines occur because, as illustrated in figure 17, the CCD array has two separate read-out lines. One line is connected to and reads out the even-numbered pixels, the other line reads out the odd-numbered pixels. Because the relative gain and offset of the analog signals from these two lines are not the same, the average normalized response and offset for the two sides are different.

Figure 18 shows the calibration setup to determine the correction for optical distortion. Each camera is mounted in turn in a test fixture 167.6 cm (66 in.) above a single LED. The LED is mounted in the center of a plate, which is fixed in position (with dowels) to the top of a computer-controlled linear X-Y stage. The camera test fixture consists of a flat plate that is leveled to approximately 0.004 cm per meter. A plumb bob, positioned in the camera test fixture, is used to align the camera with the LED. To perform a camera calibration, the plumb bob is removed and a camera is positioned on top of the plate so that the CCD array is aligned with the X stage. The LED target is stepped across from -25.4 to 25.4 cm in X and the centroid of the projected LED image is calculated at 301 equally spaced positions along the X-axis. The X- and Y-axis stage displacements are measured simultaneously with a laser interferometer.

Figure 19(a) shows a graph of the centroid estimate as a function of the stage position and a third-order curve fit to the data for sensor 3. Figure 19(b) shows the optical distortion calculated from the data in figure 19(a). From these measurements, a third-order polynomial curve fit is determined for each camera and relates the true position of the projected target image along the array (in inches) to the calculated centroid position. The coefficients of the polynomial are stored for each sensor and used to correct the centroid estimate for optical distortion in subsequent camera measurements.

System Calibration

A system calibration is performed to determine positions and angles, the principal point, and the focal length of each of the 16 cameras. The calibration LED and the computer-controlled linear

stages are shown in figures 20(a) and 20(b). A single diode is mounted to a plate attached to the computer-controlled X-Y stage and aligned with dowels. The LED is scanned in a grid measuring 10.16 by 10.16 cm. A spacer 2.54 cm (1 in.) thick and with matching dowel holes is then mounted between the stage platform and the LED plate and the LED is again scanned in a 10.16- by 10.16-cm grid. Then, a second spacer of the same thickness as the first is added and the procedure is repeated. In this way a grid of points is generated for a volume measuring 10.16 by 10.16 by 5.08 cm.

The origin of the laboratory reference frame is defined as coincident with the location of the LED when the stage is in the 0 reference position (0 in. and 0°) and a single spacer has been added. The x and y locations of the control points used during system calibration are taken to be the laser x and y measurements. The z locations of the control points are taken to be the thickness of each spacer. The corresponding camera centroid estimates of the control points are the mean centroid estimates of 100 scans at each x and y stage position. The camera parameters are the solution to the generalized least-squares problem that minimize the error in the laser measurements as well as the camera centroid estimates subject to constraint equations that fix the distance and angles between an X and Y sensor pair.

Performance Analysis

Five dominant factors affect the estimates of suspended element position and attitude:

1. SNR's of the cameras

2. Residual errors after camera calibrations

3. Proximity of one target to another within the same frame of data

4. Error in the exterior orientation parameters of the cameras either due to residual error after system calibration or to motion of the camera support structure

5. Motion of the model

Two simulations have been constructed to study the sensitivity of the position and attitude estimates to these five factors. One simulation models the digital signal of the target images and is used to determine the effect of the SNR and of sampling on the accuracy of the centroid estimate. The other simulation models the sensing geometry and tracking algorithms used in the OMS and is used to study the sensitivities of the position and attitude estimates to the five factors. The effect of each of the five factors

on the final estimate of model position is discussed next.

Camera Signal-to-Noise Ratio

Experiments on the OMS have determined the relationship between the SNR and the error in the centroid estimate. Figure 21 shows a plot of the total error, which is the sum of the standard deviation of the centroid estimate and the bias error, as a function of the SNR. The figure shows that the measured error is approximately inversely related to the SNR. Thus, as the SNR increases, the error decreases and asymptotically approaches a value of about 0.04 pixel.

A simulation has been developed to investigate the influence of the SNR and the corresponding change in the weighting factor of each target on the accuracy of the position and attitude estimates. In the simulation, the SNR for a given target was determined by calculating the difference in distance between a target and a camera, by normalizing with a reference distance, then by correcting for the falloff in light as a function of the difference between the camera pointing angle and the target pointing angle. The positions and angles of each target relative to the body reference frame are shown for the smaller element in figure 22. No other sources of error were assumed in the simulation. Figures 23(a) and 23(b) show the predicted errors in x_{cm}, y_{cm}, z_{cm}, ψ, θ, and ϕ as a function of ψ for $\psi = 0°$ to 90°; nominal values of x_{cm}, y_{cm}, $z_{cm} = 0$ in.; θ and $\phi = 0°$; and the maximum SNR = 200. Similar graphs are shown in figures 24(a) and 24(b) but with θ and $\phi = 5°$, and x_{cm}, y_{cm}, and $z_{cm} = 0$ in. In figures 25(a) and 25(b) are graphs of the error in the position and attitude of the cylinder, respectively, as a function of the standard deviation of the centroid estimate. All 16 cameras were assumed to have the same sensitivity and noise characteristics.

Residual Errors After Camera Calibration

The residual errors after calibration for optical distortion were found to be less than 0.01 pixel for all cameras. Similarly, provided a sensor has not shifted out of calibration, the residual error due to camera nonuniform responsivity has been found to be less than 0.01 pixel. Table I lists the standard deviations of the 16 camera gain and offset corrections for responsivity. The magnitude of the standard deviations is a function of the difference in the gain and offset of the two sensor readout lines.

The OMS simulation showed that the error in the position and attitude estimate due to residual camera

errors of 0.01 pixel or less is too small relative to the error due to the SNR to be distinguished from the SNR error. This situation will be the case provided the camera voltages do not drift and the calibration for responsivity does not change. However, if a sensor shifts out of calibration, that is, if the analog signals from the two lines shift relative to one another and the sensor is not recalibrated, then a residual systematic error larger than 0.01 pixel can be introduced in the centroid estimate. This systematic error is spatially periodic over the array with a period of two pixels. (See fig. 26.) The magnitude of this error will be a function of how far out of calibration the sensor has drifted. In addition to degrading camera performance, a systematic camera error of this magnitude can introduce errors in system calibration. Both errors will in turn introduce errors in the position and attitude estimate. Therefore, the cameras and associated electronics must be housed in a thermally stable environment to minimize voltage drift.

Proximity Error

As described earlier, charges are generated in each photodiode element of a CCD array in response to light striking that element and accumulating during the sensor integration period. The way in which charge is accumulated and transferred depends upon the design of the CCD sensor and can have a profound effect upon the output signal. Figure 27 shows a schematic diagram of the charge transfer process for the CCD sensor used in the OMS. After the integration period, charge that has accumulated at the photo sites (photodiode elements) is transferred in parallel to serial shift registers at the start of a read cycle. After this transfer, the next integration period begins and shifting of the charge to the output is initiated.

The efficiency with which charge is transferred along (and out) of the shift register is characterized by the charge transfer efficiency (CTE) of the CCD array. Typical values of CTE for modern CCD array designs are greater than 99.999 percent. Thus, very little signal loss occurs in the shift register. More important in this case is the efficiency of charge transfer from the photo site to the shift register. Tests of the OMS revealed a low photo site transfer efficiency (PTE) of the CCD's used in this application. As a result, not all of the charge is transferred from the photo site to the shift register during a single read cycle. Rather, some residual charge remains at the photo site that, along with the charge accumulated during subsequent integration cycles, is transferred during subsequent read cycles. Figure 28 shows a plot of the peak output signals for an LED target

image for eight consecutive read cycles in which the LED was on only for the integration period preceding the first read cycle. The plot of figure 28 is like that of a capacitive discharge curve. Similar plots have been made for different pixels along the same CCD array. The curve of figure 28 was found to vary little from pixel to pixel; rather, it showed the decay of residual charge as a function of the number of read cycles that characterize the CCD array as a whole. For the CCD arrays used in the OMS, several read cycles are required to clear the array of residual charge.

The manifestation of photo site residual charge is an afterimage or "ghost image" of a target. To clear the array of residual charge, multiple read cycles are executed at the end of the frame. The charge is then allowed to build to the background level with no target LED's illuminated. However, the time between the sampling of each target within a frame is insufficient to clear the CCD array. As a result, afterimages of the eight target LED's accumulate during any single frame. A digital filter has been incorporated in each sensor DSP to filter out these afterimages. (See fig. 29.) But, as figure 29 shows, the filtering operation is not perfect because, when two target images are in proximity, an error will be introduced in the centroid estimate. The magnitude of this proximity error will depend upon the amplitude of the afterimages and on the distances between the afterimages and the current target image.

An empirically derived function (fig. 30) is used to estimate the magnitude of the proximity error between the current target and any other target acquired within the frame. A total proximity error is determined to be the sum of these individual estimates and is added to estimates of the SNR and residual errors. Then, a weighting factor is determined for the total error estimate.

The OMS simulation was run to analyze the effect of the proximity error on the accuracies of the position and attitude estimates. Figures 31(a) and 31(b) show the error in position and attitude of the element as a function of ψ. The nominal position of the element is 0 in. with 0 angular displacement and the sensors are assumed to have a maximum uncertainty due to noise of 0.03 pixel. No other errors have been assumed.

Errors in Exterior Orientation Parameters

Errors in the exterior orientation parameters of the cameras are dominant sources of error in position and attitude estimates. Such errors will introduce both bias and random errors in the position

and attitude estimate of the suspended element for the following reasons. Sixteen camera parameters per sensing unit are solved during resection and triangulation. As a result, within the uncertainty bounds of the measurements (i.e., the x, y, and z control point locations and camera centroid estimates), several possible solutions can exist. Constraint equations have been introduced to limit the solutions to those that are compatible with the known camera geometry. Nevertheless, the camera parameters can vary, and the resulting cost function remains small.

To study the sensitivity of the position and attitude estimate to errors in the camera parameters, mean zero Gaussian random variables were added to the camera parameters and the simulation was run more than 3000 times to determine the mean and standard deviation of the resulting position and attitude estimates. Table II lists the standard deviations of the position and attitude estimates for different magnitudes of error added to the x, y, and z positions and the pointing angles of the cameras. The element was in the 0° position and for all runs and was assumed to be perfectly stationary. Table III lists the standard deviations of the position and attitude estimates for different magnitudes of error added to the x, y, and z positions of the cameras and an angular error in the pointing angles of 0.0005°; for table III, the element was in the 0° position and motion was included. A trajectory was assumed for levitation generated by the LGMSS simulation.

Tables II and III show that the accuracies of the position and attitude estimates are sensitive to errors in the camera parameters. For the 1σ value of position and attitude to remain within the specification for the OMS, the standard deviations of the errors in the camera parameters must be small (i.e., <0.0003 cm (0.0001 in.) in x^c, y^c, and z^c and <0.001° for the pointing angles).

Camera motion during target acquisition will introduce additional errors in the position and attitude estimate of the suspended element. Unlike the residual error after system calibration, which introduces both a bias and a random error in the position estimate, the error introduced by camera motion will vary in time and will be a function of the modes of vibration of the camera support structure. Finite element analyses have been performed to predict motion of the support structure. Accelerometer measurements were made of the floor of the building that will house the LGMSS and the power spectral density of the disturbance input was calculated. This information, together with the finite element model, yielded a maximum predicted displacement along the

z direction of approximately ±0.0004 cm (0.0002 in.) for the first mode.

Model Motion

Because the target LED's are turned on sequentially, the position of each target LED is determined at a different point in time. In the tracking algorithm, the suspended element is assumed stationary as the positions of the eight target LED's are acquired. To correct for target motion during signal acquisition, a time interpolation algorithm is used. The location of each LED within a frame is interpolated in time based on the four previous frames; then, the positions of all eight LED's are estimated at the time the first LED within the frame was turned on. Without a correction for motion of the suspended element between acquisition of each target, the error in the position and attitude estimate grows rapidly as a function of integration time and rate of element displacement. Even with a correction, the error in the position and attitude estimate grows as a function of integration time and frame time.

As an example of the effect of model motion on the error in the position and attitude estimate, table IV shows the standard deviations of predicted errors in the trajectories of the element based on a model of the plant and control system for the magnetic suspension system under three conditions: suspension about the 0° position, release by the mechanical injection device, and a commanded yaw displacement at 1.0° per second. Figures 32(a)–(f) show the input trajectory for the second case, which involved release by the mechanical injection device. For the results depicted in table IV, the time between frames is 25 msec and the integration time is 2 msec. A minimum 1σ uncertainty of 0.03 pixel was assumed for the centroid estimate; and uncertainties of 0.0003 cm and 0.0001° (1σ) were assumed in the x, y, and z positions of the cameras. A comparison of the results of tables II and III, which were obtained assuming no motion for the model, with the results of table IV, in which interpolation was used, shows that motion of the model increases the errors in the estimates of position and attitude by about a factor of 2.

Experimental Results

Several experiments have been run on the OMS to determine system accuracy and the effects of different calibration parameters and errors on the final system performance. Three principal experiments were run to assess overall system accuracy. In the first experiment, the average x_f, y_f, and z_f positions of a single

LED are measured at 100 locations in a 10 by 10 grid measuring 10.16 by 10.16 cm.

The position measurements of the first experiment are shown in figures 33 and 34. Figures 33(a) and 33(b) show the differences between the x_f or y_f OMS-predicted LED coordinates and the laser system plots of the x_f or y_f values. The values of z predicted by the OMS over the whole grid are shown plotted in figure 33(c). The standard deviations of the x_f, y_f, and z_f estimates ranged from <0.0005 cm (<0.0002 in.) to 0.001 cm (0.0004 in.) over the grid of points. The maximum standard deviations of x_f, y_f, and z_f predicted by the OMS simulation over the same grid for a minimum 1σ uncertainty of 0.03 pixel for the centroid estimate and a 1σ uncertainty of 0.0003 cm in the camera parameters are 0.001 cm (0.0005 in.) for x_f and y_f and 0.002 cm (0.0008 in.) for z_f.

In the second experiment, a half-model of the cylinder is mounted on top of a rotary stage that is affixed to the x and y linear stages. (See fig. 34.) The yaw, pitch, and roll axes are aligned with a laser; and the x, y, and z positions of the model are determined from the x and y laser interferometer measurements and the distance between the center of rotation and the origin of the coordinate system. The body coordinates of the targets are taken to be the x_f, y_f, and z_f OMS-predicted target locations of the model aligned at ψ, θ, and $\phi = 0°$ and at a displacement of x and $y = 0$ in. for the linear stages. The body coordinate system is assumed to be coincident with the laboratory coordinate system and, after the x_f, y_f, and z_f locations of the targets are determined, these values are read into the tracking algorithm as the x_b, y_b, and z_b target locations. The model is then moved ±1.27 cm (0.5 in.) in x and y and measurements are taken over a 10 by 10 grid to determine OMS accuracy for small displacements.

The results of the second experiment are shown in figures 35 and 36. The error in the estimates of x_{cm}, y_{cm}, and z_{cm} versus the difference between the laser measurements and the OMS estimates is plotted in figure 35. Figure 36 shows the standard deviations of the estimates. The standard deviations of the OMS-predicted position and attitude estimates using a minimum 1σ uncertainty of 0.03 pixel in the centroid estimate and a 1σ uncertainty of 0.0003 cm in the camera parameters are $x_{cm} = 0.0013$ cm (0.0005 in.), $y_{cm} = 0.0015$ cm (0.0006 in.), $z_{cm} = 0.0025$ cm (0.0001 in.), $\psi = 0.002°$, $\theta = 0.004°$, and $\phi = 0.048°$.

In the third experiment, the repeatability of the OMS is determined. The element is aligned at x, y, and $z = 0$ in. and ψ, θ, and $\phi = 0°$. The rotary stage is set to 0° and the OMS output is noted in all six degrees of freedom. The element is rotated in 10° increments to $\psi = 180°$ (on the rotary stage) and the position and attitude are recorded for each yaw location. The element is rotated back to $\psi = 0°$ and the position and attitude are recorded. This procedure is repeated 20 times and the positions and attitudes are recorded for each yaw location. The repeatability of the OMS was found to be better than x, y, and $z = 0.0025$ cm (0.001 in.); ψ and $\theta \approx 0.005°$; and $\phi \approx 0.01°$.

Concluding Remarks

An optical measurement system (OMS) has been designed and tested for the large gap magnetic suspension system (LGMSS) that is being used at Langley Research Center. The LGMSS is to be used to test control laws for magnetic suspension systems for aerospace applications of vibration isolation and pointing. The hardware design, signal flow, and details of the tracking algorithm and calibration techniques have been examined; also, system requirements were reviewed and a performance analysis done based on simulations and experiments.

The OMS is based on point target-tracking techniques and uses 16 linear charge-coupled device (CCD) cameras to detect the locations of small infrared light-emitting diodes (LED's) on a cylindrical element that is equipped with a permanent magnet core. The location of the projected image of an LED in a camera is determined as the position of the centroid of the light distribution falling on the CCD array. High-speed analog-to-digital converters and digital signal processors are used to digitize the video signal and compute the centroid location from the digitized signal. Based on the locations of the projected images of the LED's in the cameras, the sensing system estimates the position and attitude of the suspended element and supplies this information to the LGMSS controller.

The OMS has been calibrated and experiments have been conducted to evaluate system accuracy. Experiments designed to determine the accuracy of point tracking revealed that the system can determine the x, y, and z location of a target within 0.001 cm (0.0005 in.) within a volume of 10.16 by 10.16 by 5.08 cm (4 by 4 by 2 in.). Based on a simulation model of the OMS, camera signal-to-noise ratios consistent with measured values on the actual system, and an uncertainty in the camera parameters of 0.0003 cm (0.0001 in.), the predicted standard deviations of the axial estimates of points within the volume were 0.001 cm (0.0005 in.). Results of initial experiments on a model of the suspended element

showed the system in the 0 reference position (0 in. and 0°) to be accurate within 0.0025 cm (0.001 in.) for the origin of the body in the laboratory reference frame, within 0.005° for pitch and yaw, and within 0.1° for roll. These same experiments revealed that the position and attitude estimate is sensitive to the position and attitude of the suspended element and that the accuracy will degrade for small pitch or roll angles and element translations >1 cm. The simulation and the experiment agreed closely in predicting the position and attitude of the suspended element.

Additional tests should be conducted on the system to understand the effect of calibration and test techniques on the measured accuracies of position and attitude. In addition, a full analysis should be made to determine the effect of motion of the suspended element.

NASA Langley Research Center
Hampton, VA 23681-0001
March 11, 1994

References

1. Tuttle, Marie H.; and Kilgore, R. A.: *Magnetic Suspension and Balance Systems — A Comprehensive Annotated Bibliography.* NASA TM-4318, 1991.

2. Groom, Nelson: *Description of the Large Gap Magnetic Suspension System (LGMSS) Ground-Based Experiment.* Aerospace Applications of Magnetic Suspension Technology, N. J. Groom and C. P. Britcher, eds., NASA CP-10066, Part 2, 1991. pp. 365–377.

3. Boom, R. W.; Abdelsalam, M. K.; Eyssa, Y. M.; and McIntosh, G. E.: *Repulsive Force Support System Feasibility Study.* NASA CR-178400, 1987.

4. Tcheng, Ping; and Schott, Timothy D.: A Five Component Electro-Optical Positioning System. ICIASF '87 Record International Congress on Instrumentation in Aerospace Simulation Facilities, IEEE, 1987, pp. 322–333.

5. Brown, Duane C.: STARS (*S*imultaneous *T*riangulation *A*nd *R*esection *S*ystem), A Turnkey System for Close Range Photogrammetry. Presented at Symposium: Precision and Speed in Close Range Photogrammetry (York, England), Sept. 1982.

6. Brown, Duane C.: *Application of Close-Range Photogrammetry to Measurements of Structures in Orbit,* Volume 1. GSI Tech. Rep. No. 80-012 (Contract No. MOM7DNS-895942), Geodetic Services Inc., Sept. 15, 1980.

7. Welch, Sharon S.: *Effects of Window Size and Shape on Accuracy of Subpixel Centroid Estimation of Target Images.* NASA TP-3331, 1993.

8. Wong, K. W.: Basic Mathematics of Photogrammetry. *Manual of Photogrammetry,* 4th ed., Chester C. Slama, Charles Theurer, and Soren W. Henriksen, eds., Am. Soc. Photogramm., 1980, pp. 37–101.

9. Golub, Gene H.; and Van Loan, Charles F.: *Matrix Computations,* Second ed. Johns Hopkins Univ. Press, 1989.

Table I. Standard Deviations of Gain and Offset Corrections for All 16 Cameras

Gain	0.78	.43	.27	.32	.27	.42	.27	.99	2.5	1.7	.51	.36	1.9	.28	.33	.36
Offset	4.2	2.3	2.3	2.6	1.3	5.1	1.5	2.2	12.0	5.4	2.8	2.2	2.8	1.6	1.4	1.9

Table II. Standard Deviations Predicted by Simulation for Different
Values of Assumed Uncertainty in Camera Positions

[Camera resolution was assumed to be 0.03 pixel for peak SNR and cylinder was stationary]

No motion for —		Standard deviation of error for—					
Δ positions, cm	Δ angles, deg	x_{cm}, cm	y_{cm}, cm	z_{cm}, cm	ψ, deg	θ, deg	ϕ, deg
0.0003	0.0001	0.0005	0.0008	0.0003	0.001	0.002	0.02
.0003	.0005	.0008	.0010	.0003	.002	.003	.03
.0005	.0001	.0008	.0008	.0003	.001	.002	.02
.0005	.0005	.0008	.0010	.0003	.002	.003	.02
.0003	.001	.0013	.0015	.0008	.003	.004	.04

Table III. Standard Deviations Predicted by Simulation for Different Values of Assumed Uncertainty
in x, y, and z Positions of Cameras Given That Cylinder is Undergoing Motion

[Simulated input trajectory was steady-state suspension; angular uncertainty was 0.0005°
for all three cases; camera resolution was assumed to be 0.03 pixel for peak SNR]

Standard deviation of uncertainties in position of cameras, cm	Standard deviation of error for—					
	x_{cm}, cm	y_{cm}, cm	z_{cm}, cm	ψ, deg	θ, deg	ϕ, deg
0.0003	0.0013	0.0013	0.0005	0.004	0.004	0.05
.0004	.0013	.0013	.0018	.008	.015	.07
.0005	.0015	.0015	.0020	.009	.018	.09

Table IV. Standard Deviations for Position and Attitude Variables Predicted
by Simulation for Different Simulated Trajectories of Suspended Element

[Camera resolution was assumed to be 0.03 pixel for peak SNR; standard deviation of error in x, y, and z
positions of cameras was assumed to be 0.0003 cm; angular uncertainty was 0.0005° in all cases]

Conditions	1σ uncertainty for—					
	x, cm	y, cm	z, cm	ψ, deg	θ, deg	ϕ, deg
Levitation	0.0013	0.0013	0.0005	0.004	0.004	0.05
Launch	.0014	.0014	.0004	.004	.004	.05
Commanded yaw displacement of 1°	.0014	.0015	.0004	.002	.004	.05

14
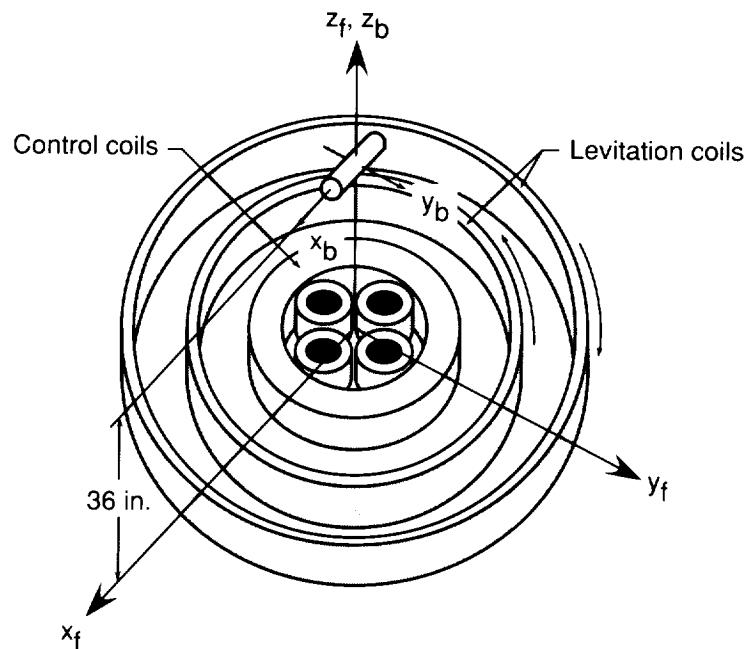
Figure 1. Cylindrical element suspended by planar array of electromagnets.
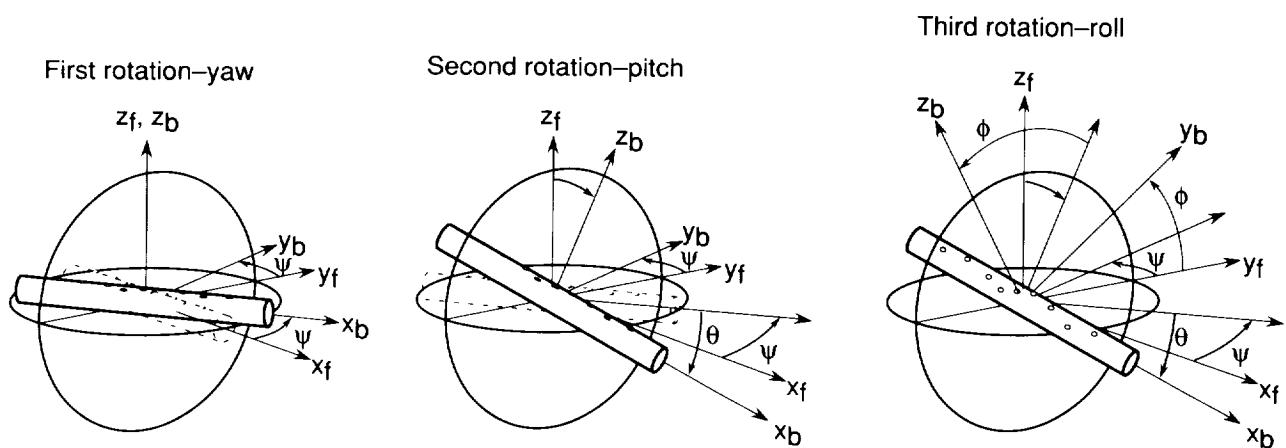
Figure 2. Rotation sequence for Euler angles ψ, θ, and ϕ.
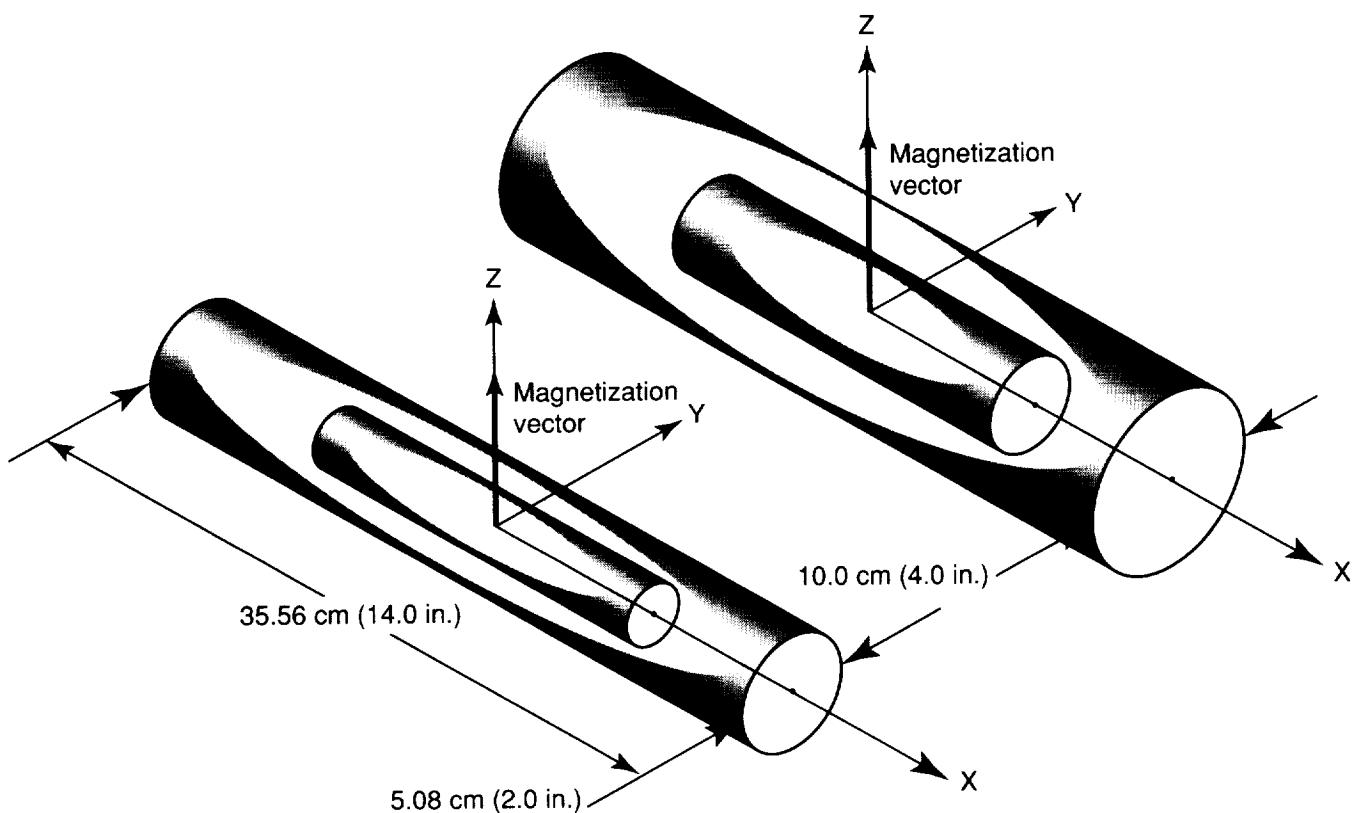
Figure 3. Orientations of core magnetization vectors and sizes of cylindrical elements.

16
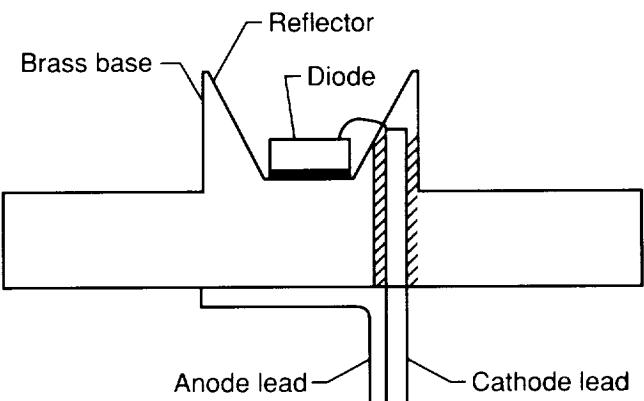
(a) Schematic of LED target.
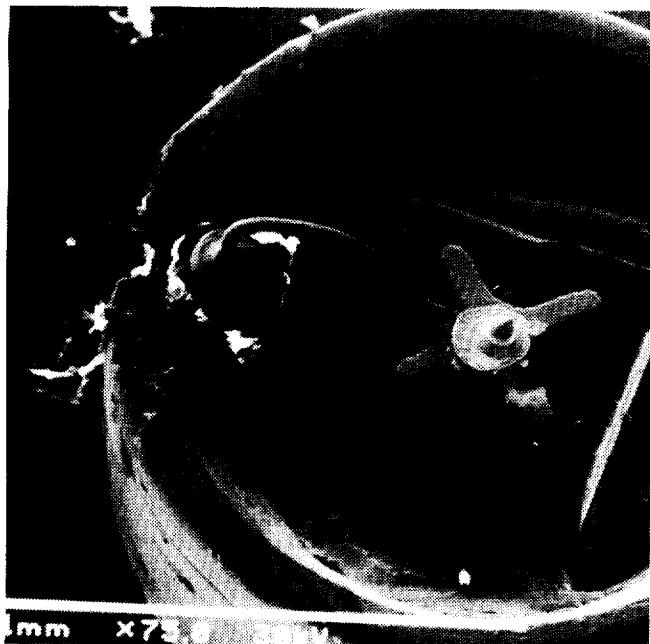
(b) LED target magnified 75 times.

(c) LED target size.

L-90-4666

Figure 4. Diagram and photographs of LED target.
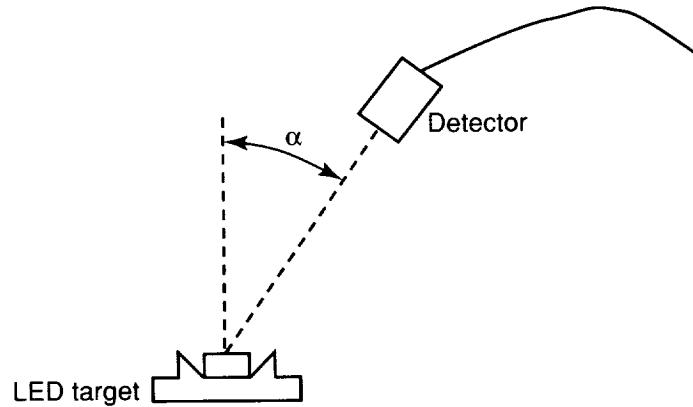
(a) Geometry of LED target and detector during experiment to measure light output.
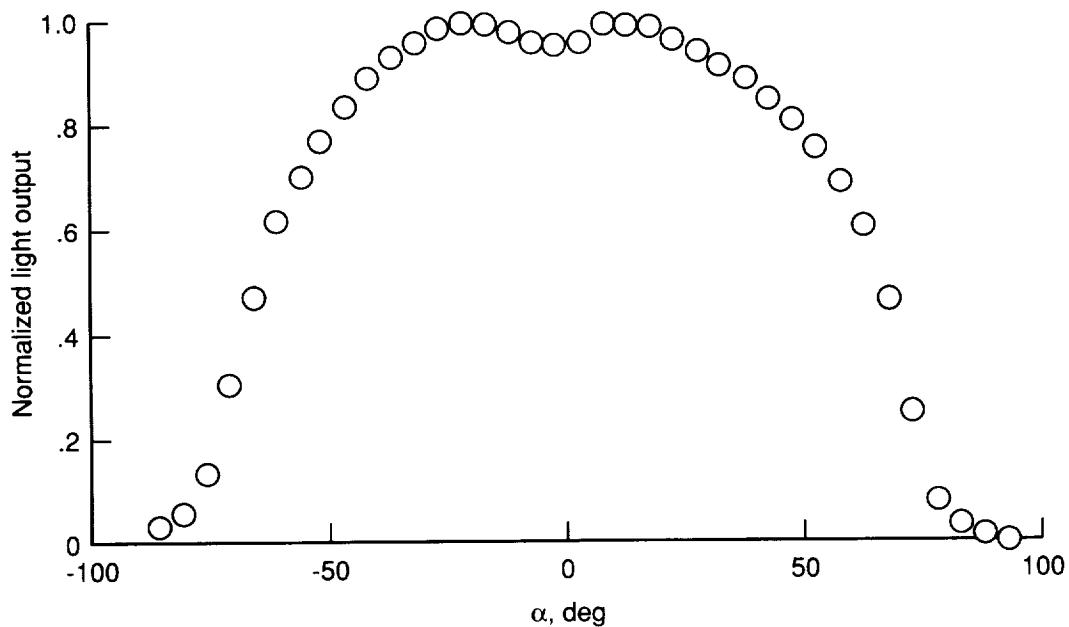
(b) Normalized light output of LED target as function of angle.

Figure 5. Target geometry and target light output.
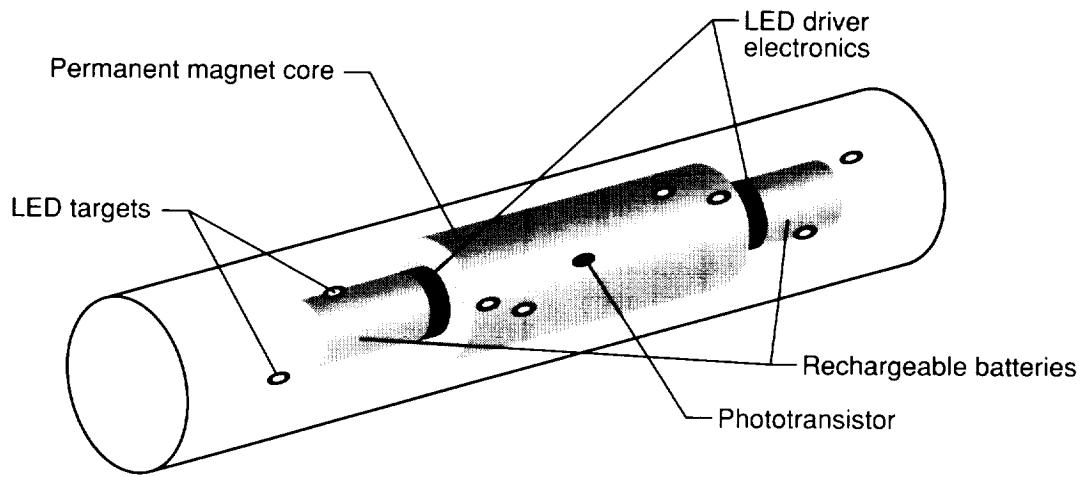
Figure 6. Locations of LED targets, driver electronics, permanent magnet core, and LED power supply in cylindrical element.
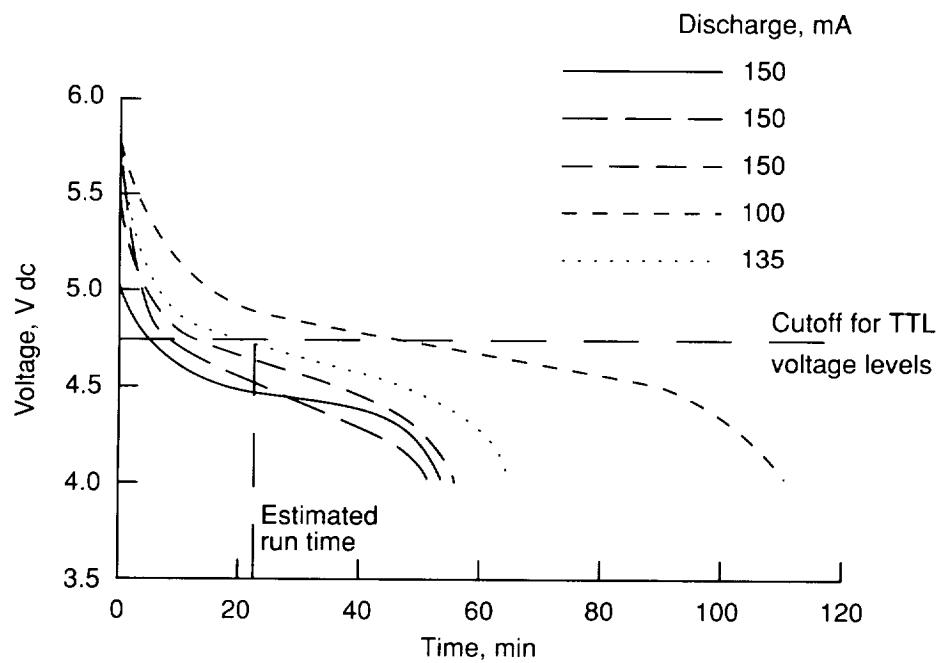
Figure 7. Battery voltages as function of time and discharge rates.

Interval	Data acquisition			Camera DSP	MATH DSP	
1	Diode 1 (D1)	Integration time	Sample D1			
2	Diode 2 (D2)	(a)		Calculate D1 centroid		
3	Diode 3 (D3)	(a)			Calculate D1 x, y, z	
4	Diode 4 (D4)	(a)				
5	Diode 5 (D5)	(a)	One frame			
6	Diode 6 (D6)	(a)				
7	Diode 7 (D7)	(a)				
8	Diode 8 (D8)	(a)	Sample D8			
9				Calculate D8 centroid		
10					Calculate D8 x, y, z	
11						Calculate suspended element x, y, z, ψ, θ, and ϕ — transfer data
12						

a Variable time required to process image.

Figure 8. Software structure and timing used during tracking.
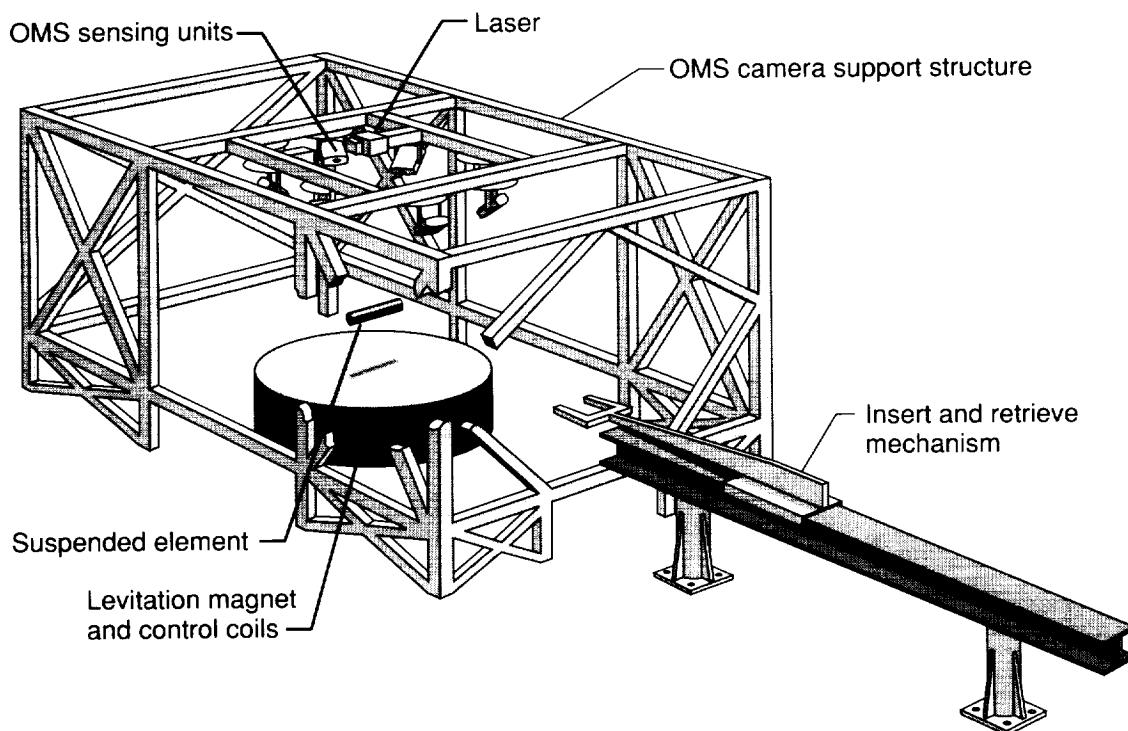
Figure 9. LGMSS and OMS.
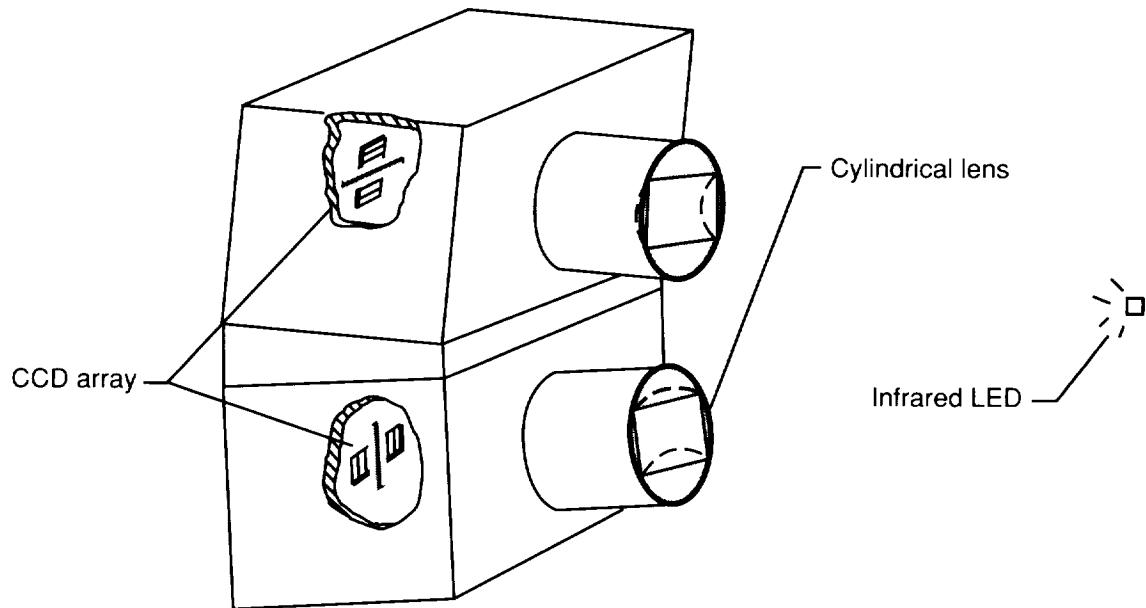
(a) Two linear CCD cameras oriented orthogonally with wedge between.
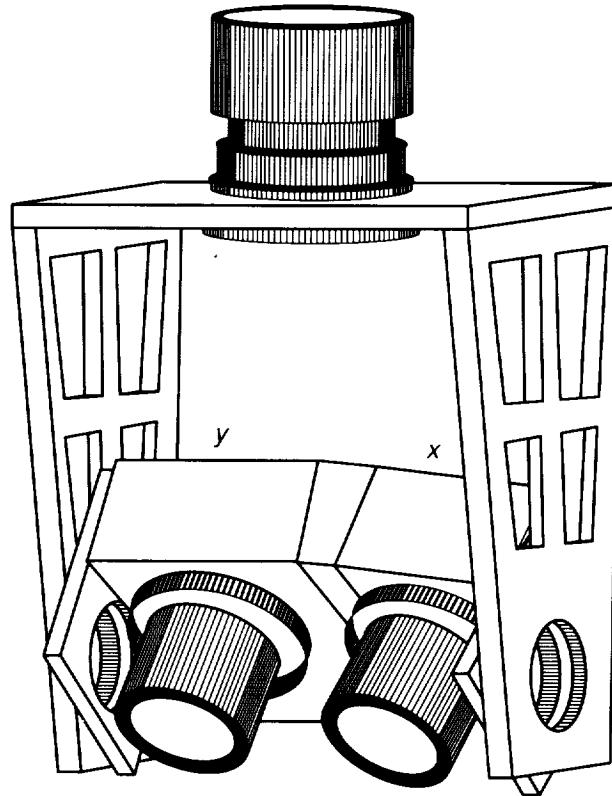
(b) Sensing unit in mount; y denotes location of y camera and x denotes the location of the x camera.

Figure 10. Sensing unit.
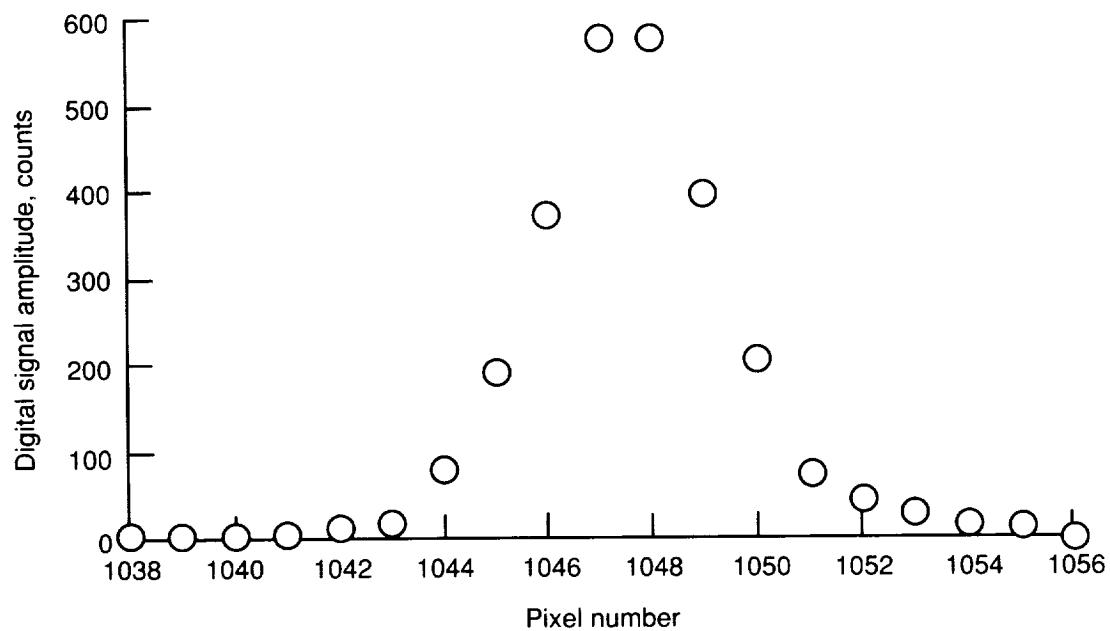
Figure 11. Digital output of camera 3 expanded to show signal distribution of LED target. Image was acquired with camera mounted 64 in. directly above LED target.
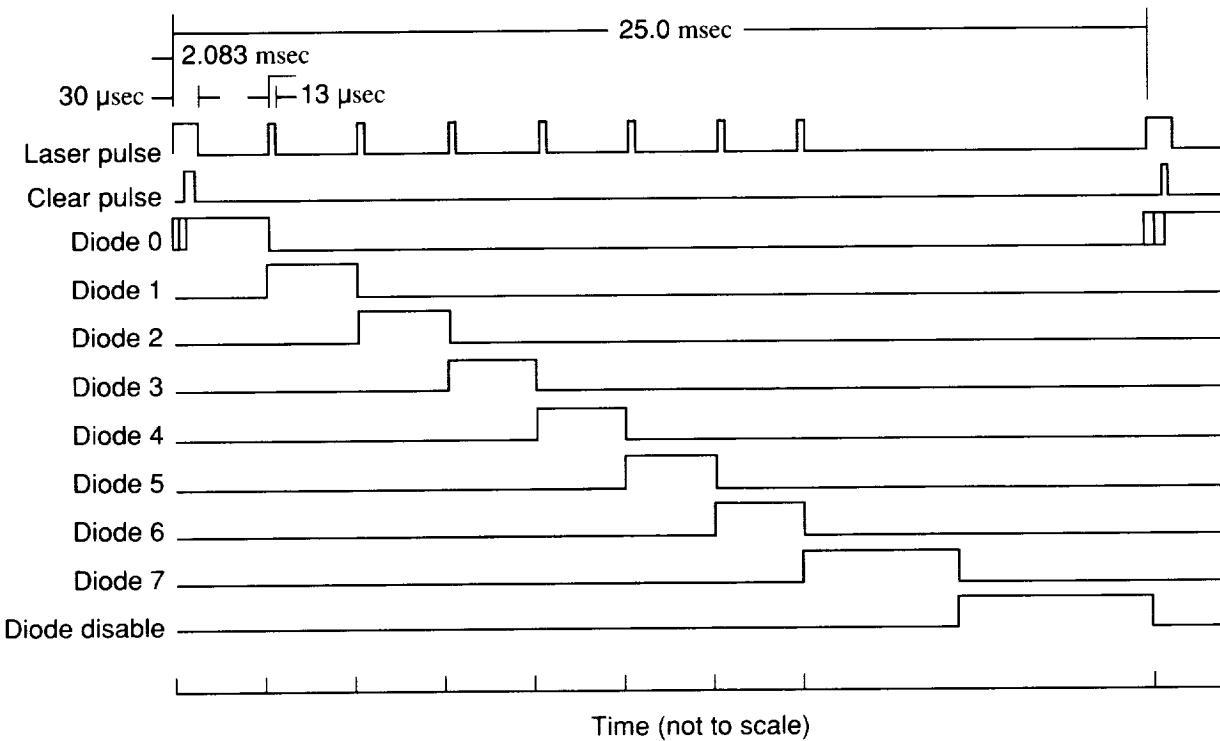
Figure 12. Target illumination sequence and time allocated for computing position and attitude of suspended element.
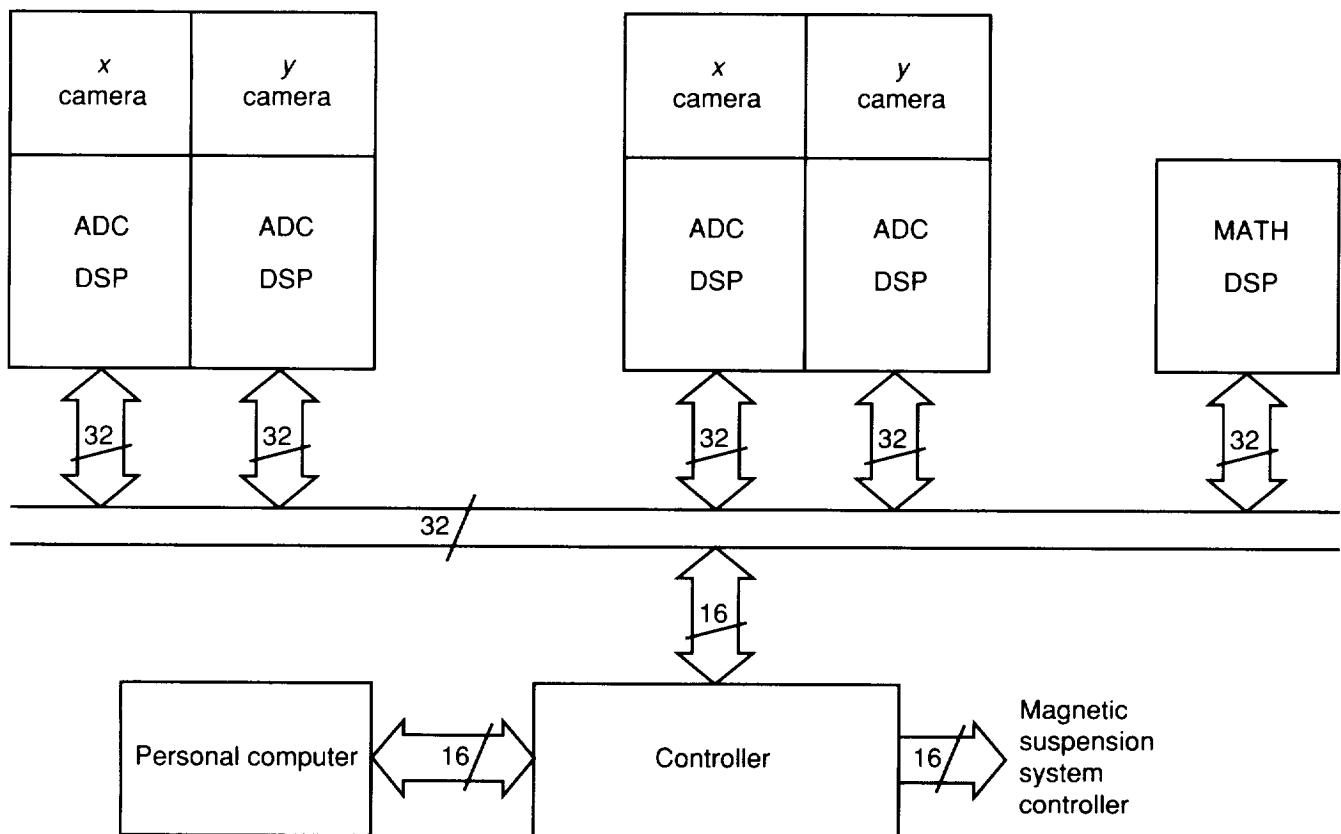
Figure 13. Signal flow in OMS.

Start

Read image
data

Search every third
pixel for peak
location, PK_LOC

Is
PK_LOC
>50 or
<1999
?

No

Set error flag

Yes

Search ±10
pixels about peak
for new peak location

Correct data for
pixel nonuniformity

Search ±40
pixels about peak
for new peak location

PK_LOC = New peak
location

Calculate second moment
$\bar{\sigma}$ for ±30 pixels
about PK_LOC

$N = \bar{\sigma} + 1$

Calculate centroid $\bar{x}$

$$\bar{x} = \frac{\displaystyle\sum_{n = PK\_LOC - N}^{n = PK\_LOC + N} n\, I(n)}{\displaystyle\sum_{n = PK\_LOC - N}^{n = PK\_LOC + N} I(n)}$$

Figure 14. Centroiding algorithm.

24
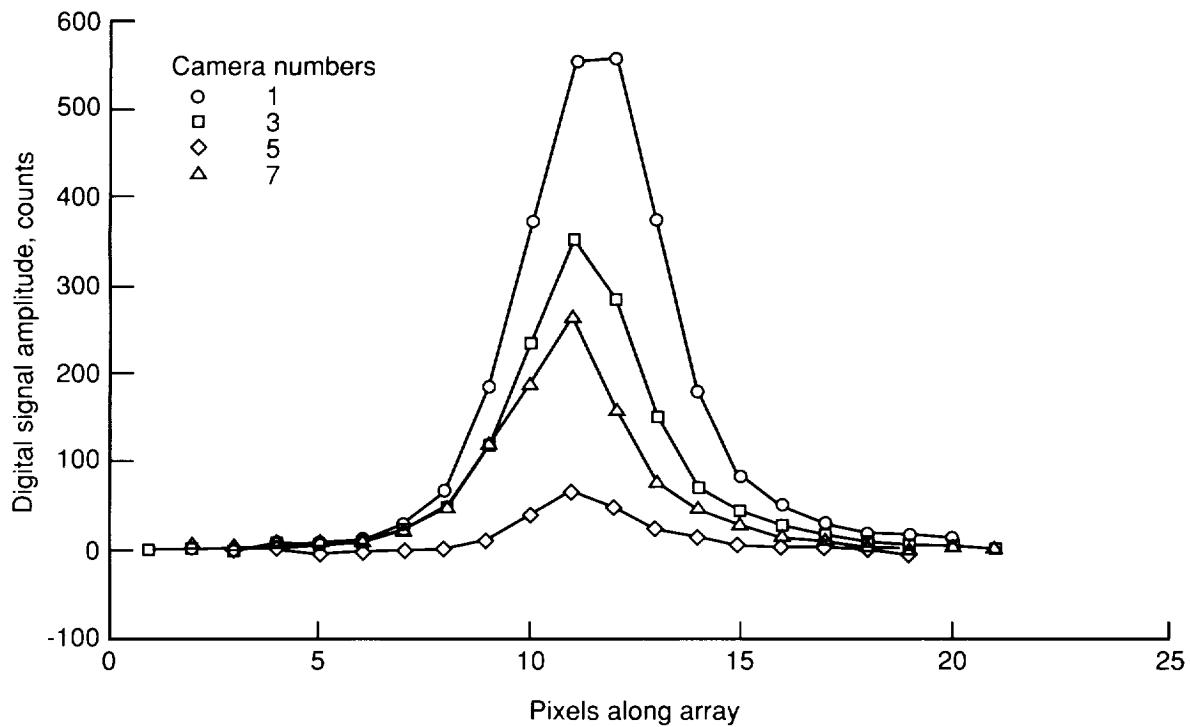
Figure 15. Expanded digital signals corresponding to light-intensity distributions for images of targets as viewed from sensor 7 in OMS. All images have been referenced to same peak pixel location to illustrate range of sizes and shapes of sampled image distributions generated by different targets.
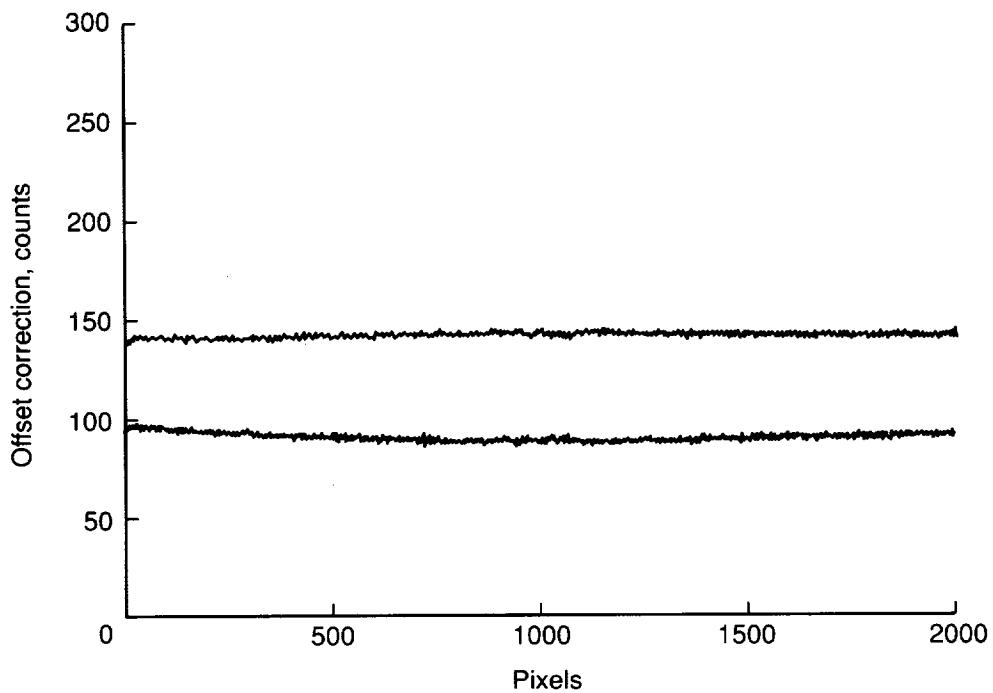
(a) Offset correction for sensor 5.
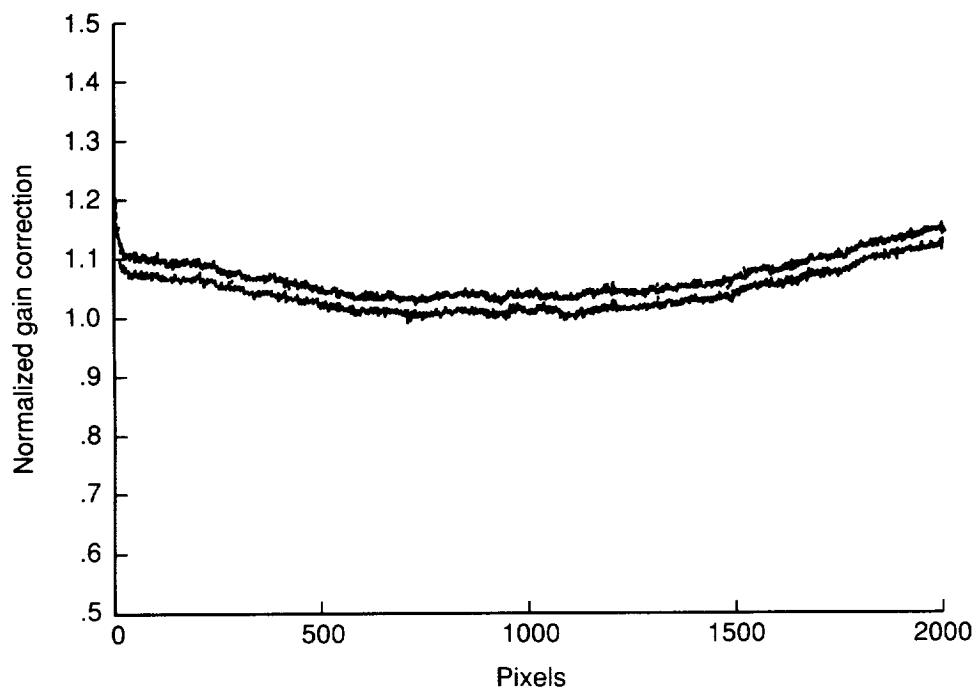
(b) Normalized gain correction for sensor 5.

Figure 16. Representative sensor correction and offset.
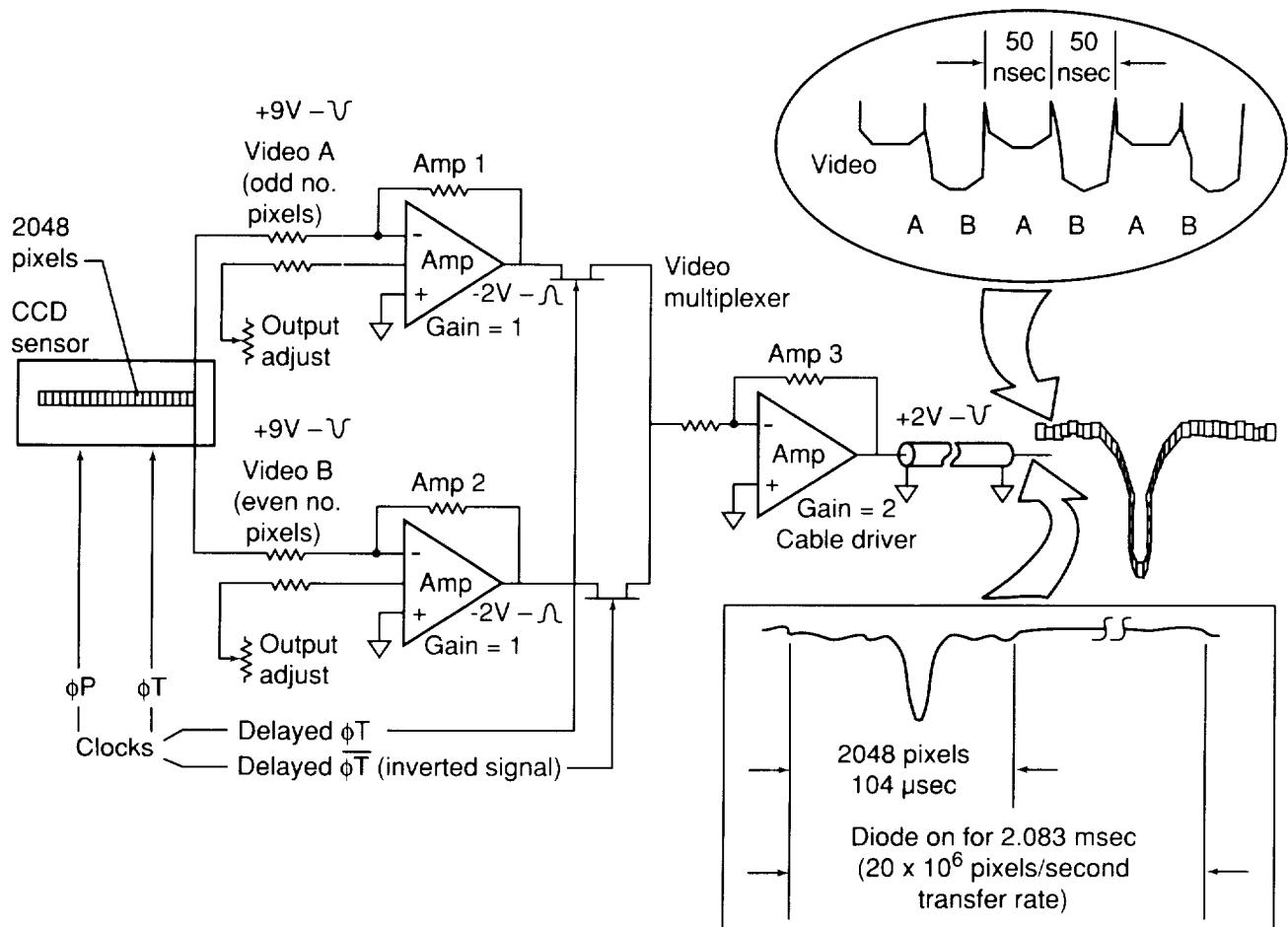
Figure 17. Camera analog circuitry and two output signals.

L-91-16508
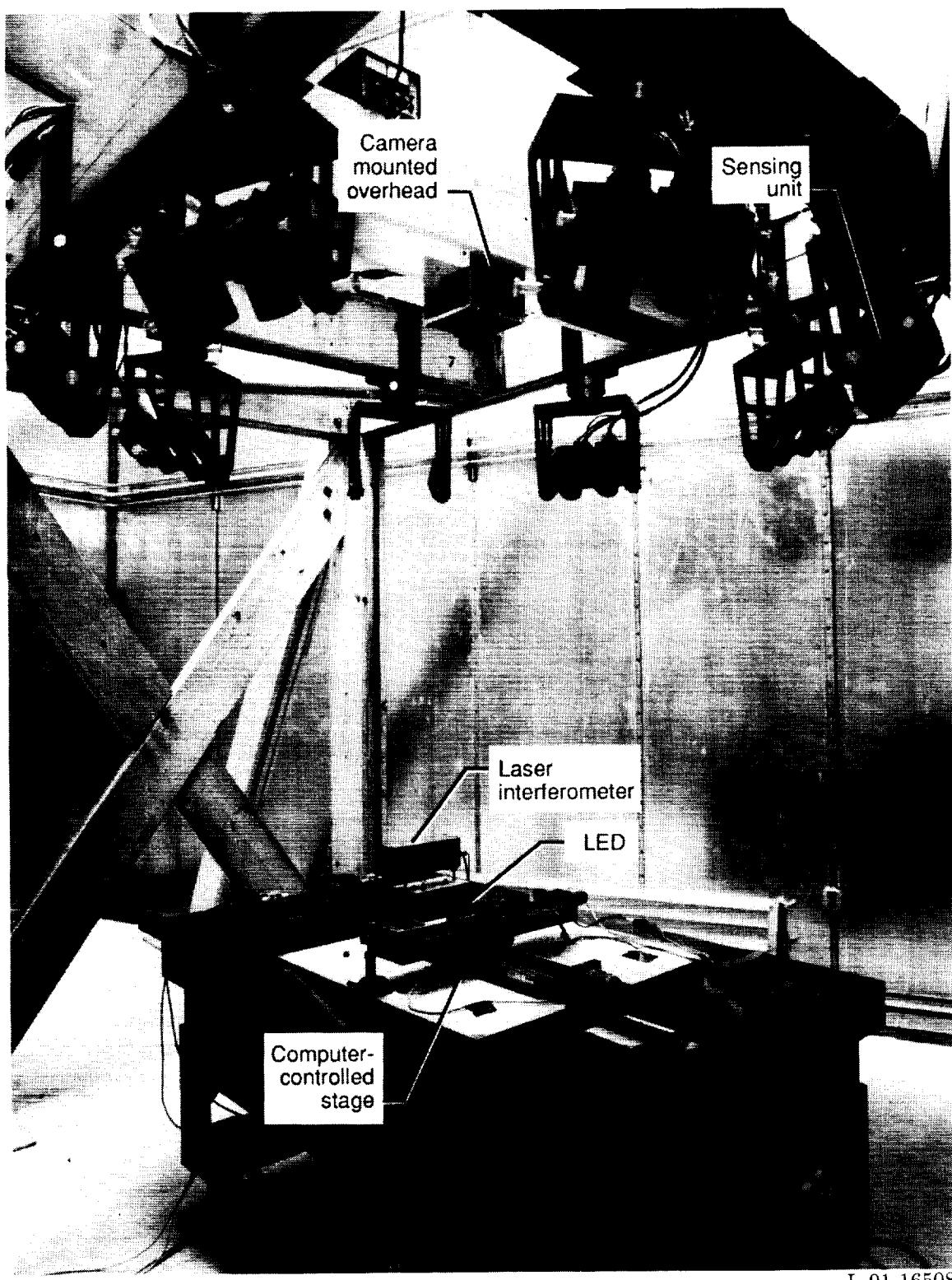
Figure 18. Experimental setup with overhead camera, LED, and computer-controlled linear stage.
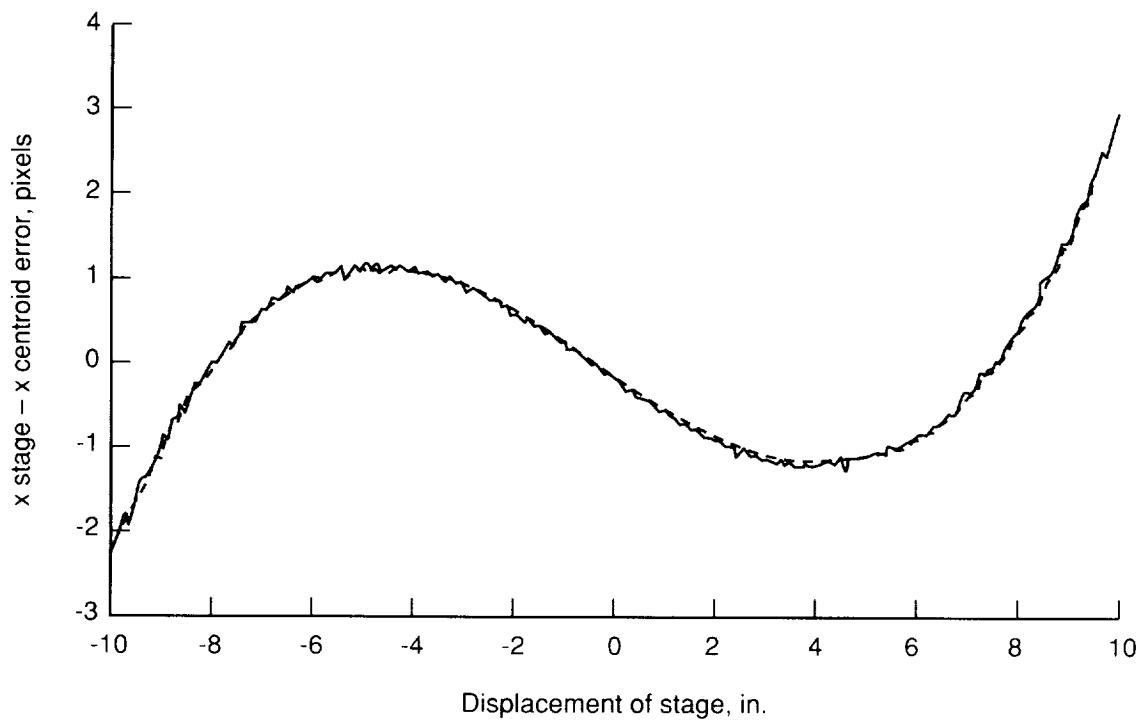
(a) Centroid estimate versus position of computer-controlled linear stage and third-order curve fit to data.
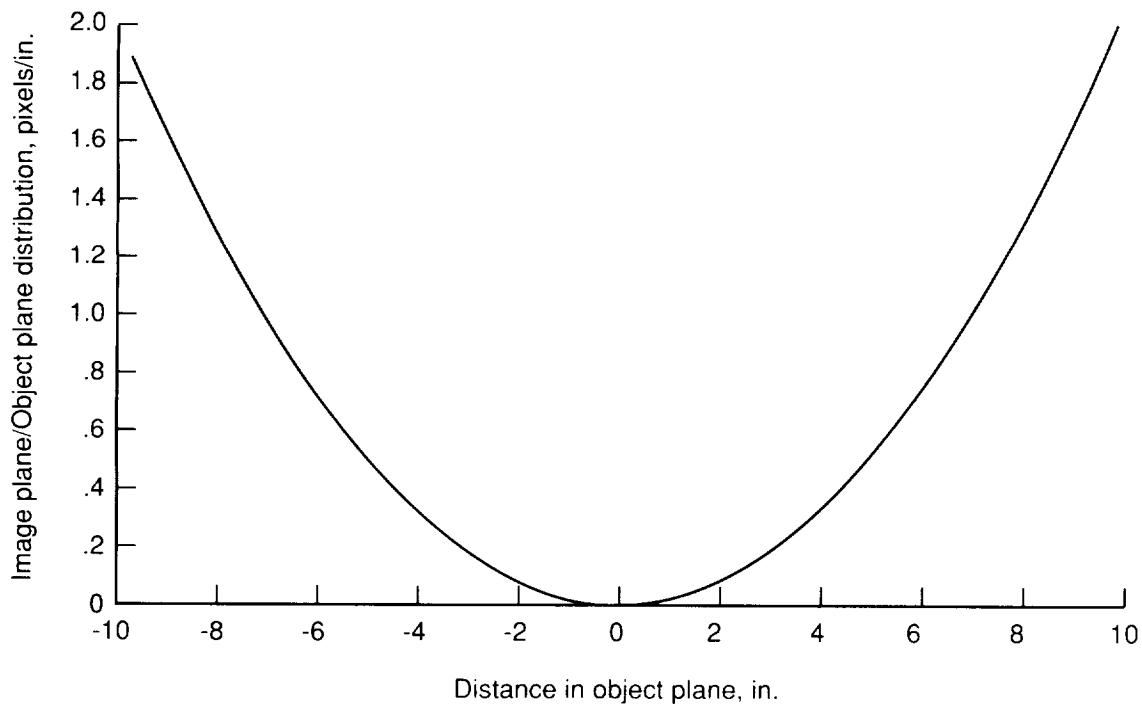
(b) Optical distortion scaled to dimensions of object plane.

Figure 19. Readings from sensor 3.

Sensing units

LED

Laser measurement system

Spacer

Computer-controlled stages (x and y)
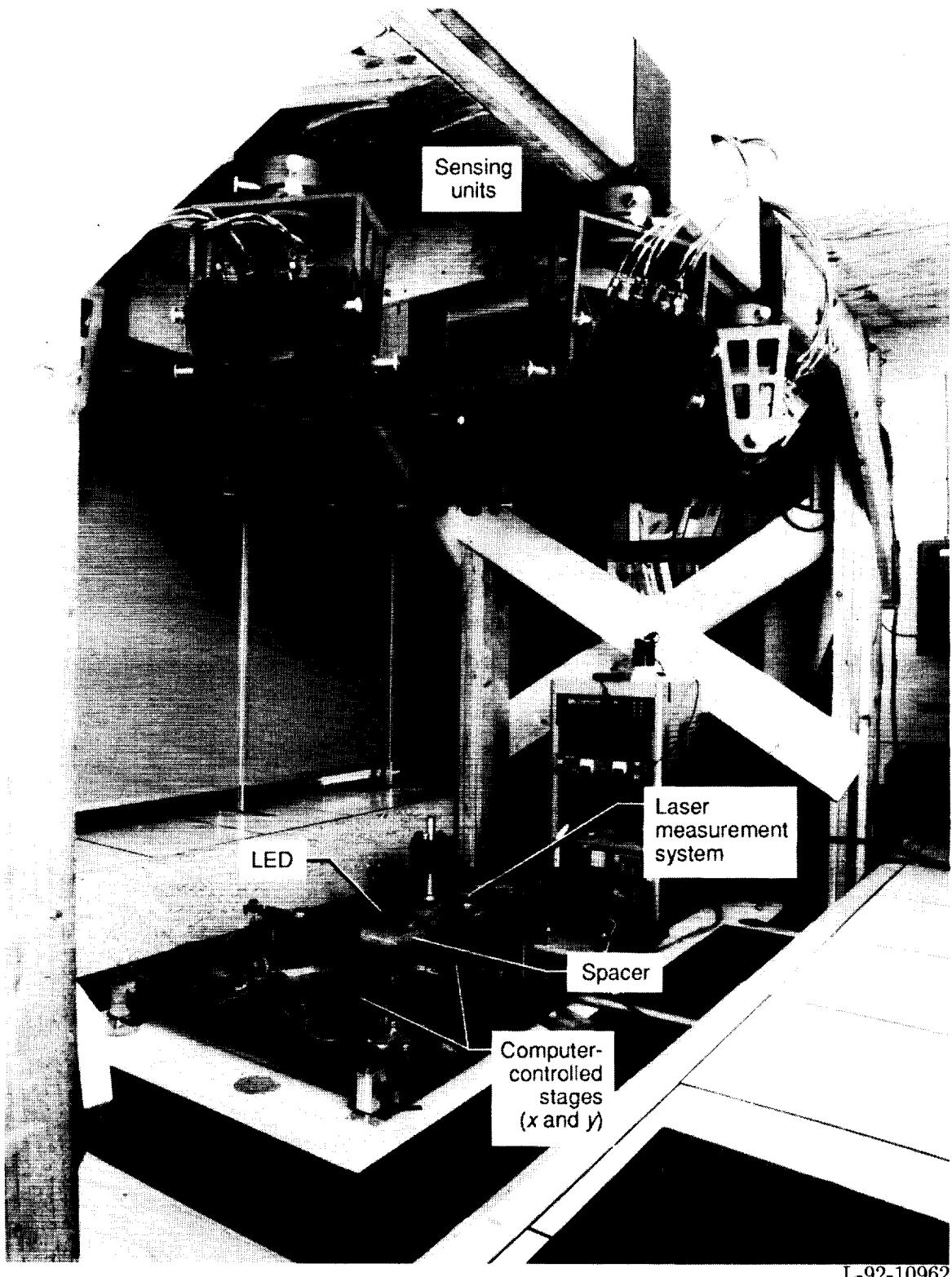
L-92-10962

(a) Calibration setup.

Figure 20. Experimental apparatus.
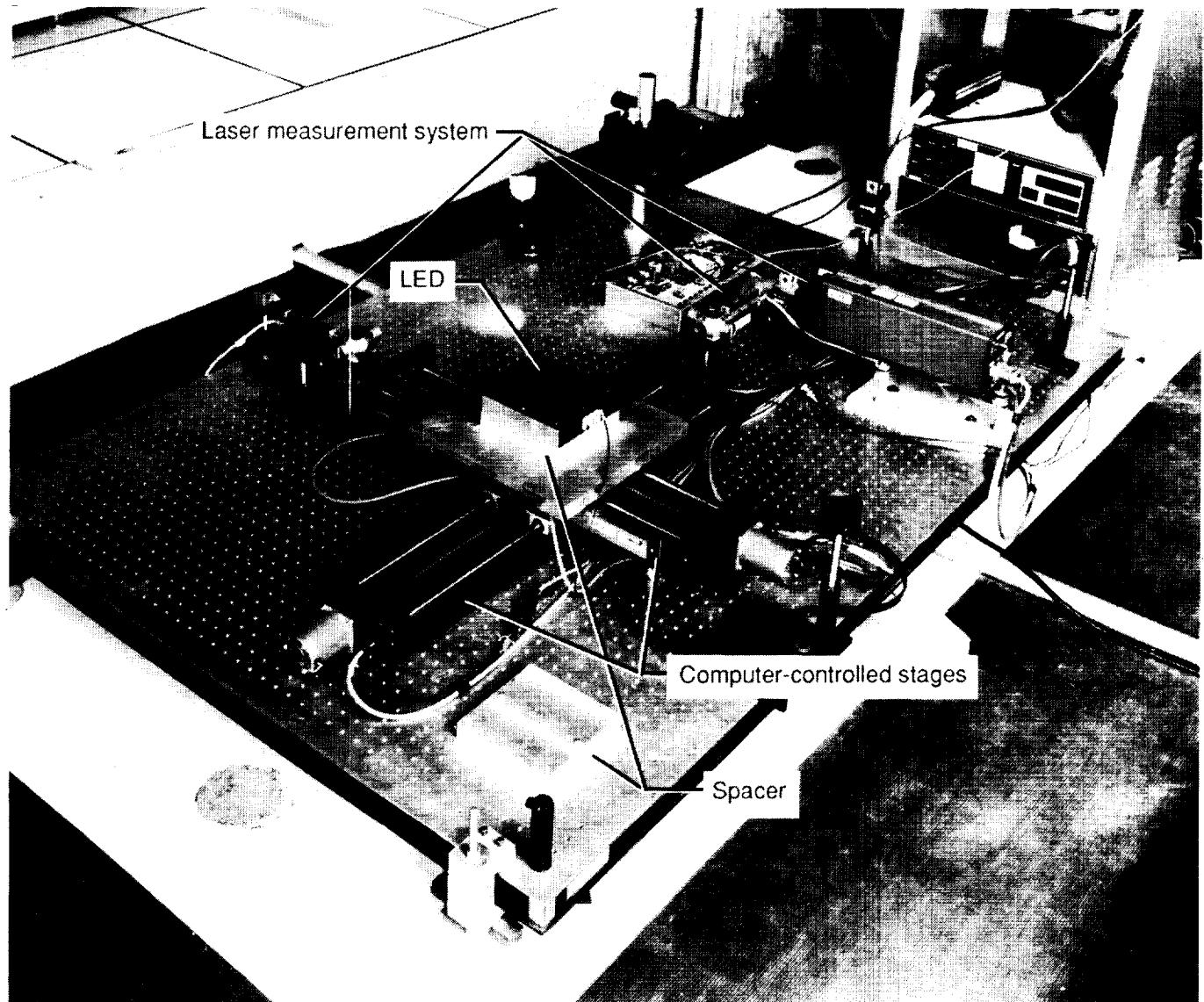
L-92-10963

(b) Closeup of LED stage mount.

Figure 20. Concluded.
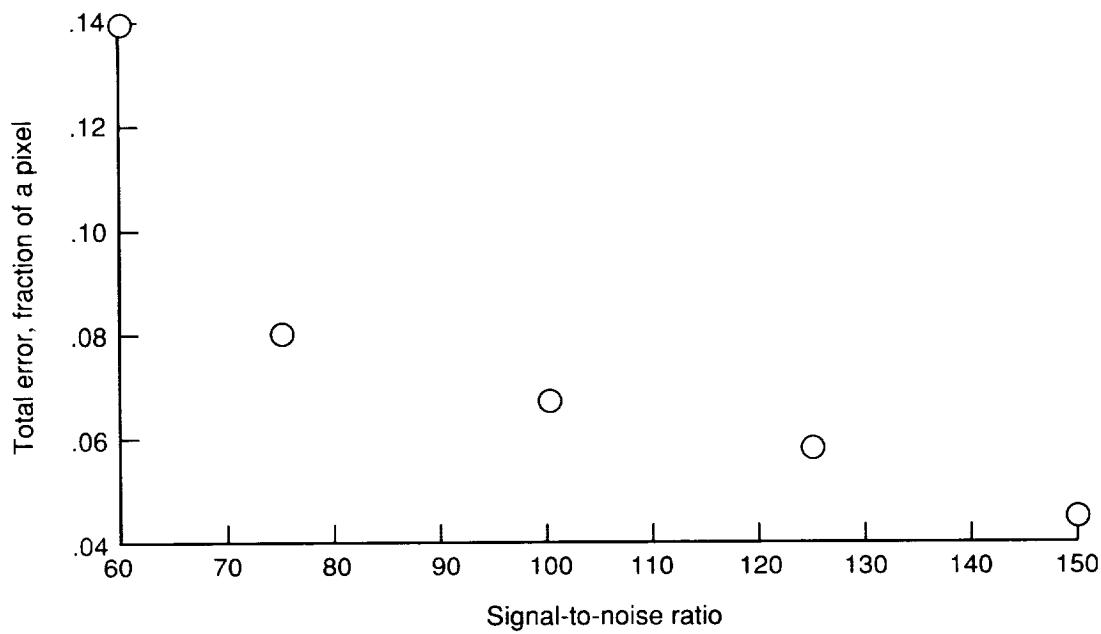
Figure 21. Total error in centroid estimate as function of SNR for sensor 7.
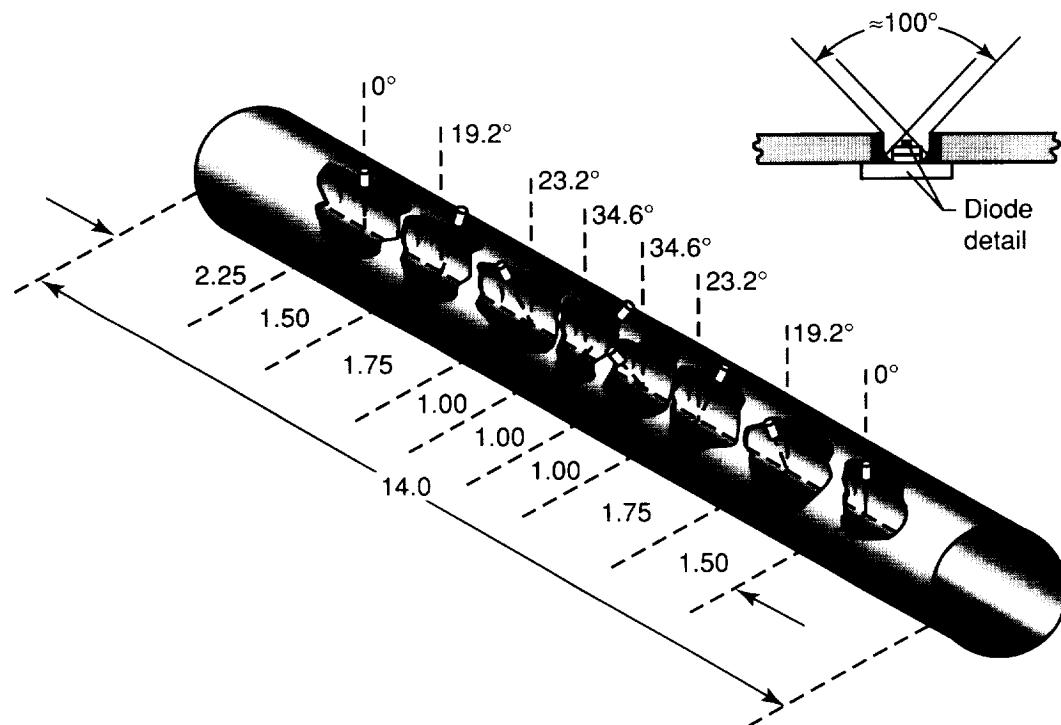
Figure 22. Positions and angles of eight target LED's on smaller element. All linear dimensions are in inches.
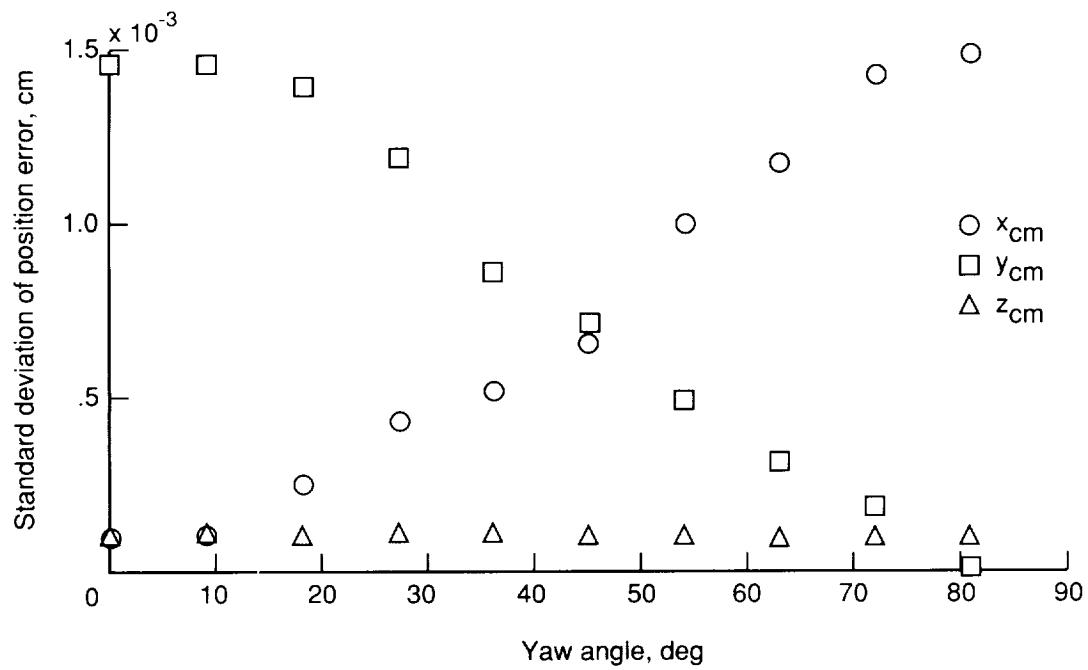
(a) Predicted error as function of yaw angle (maximum centroid accuracy assumed to be 0.03 pixel).
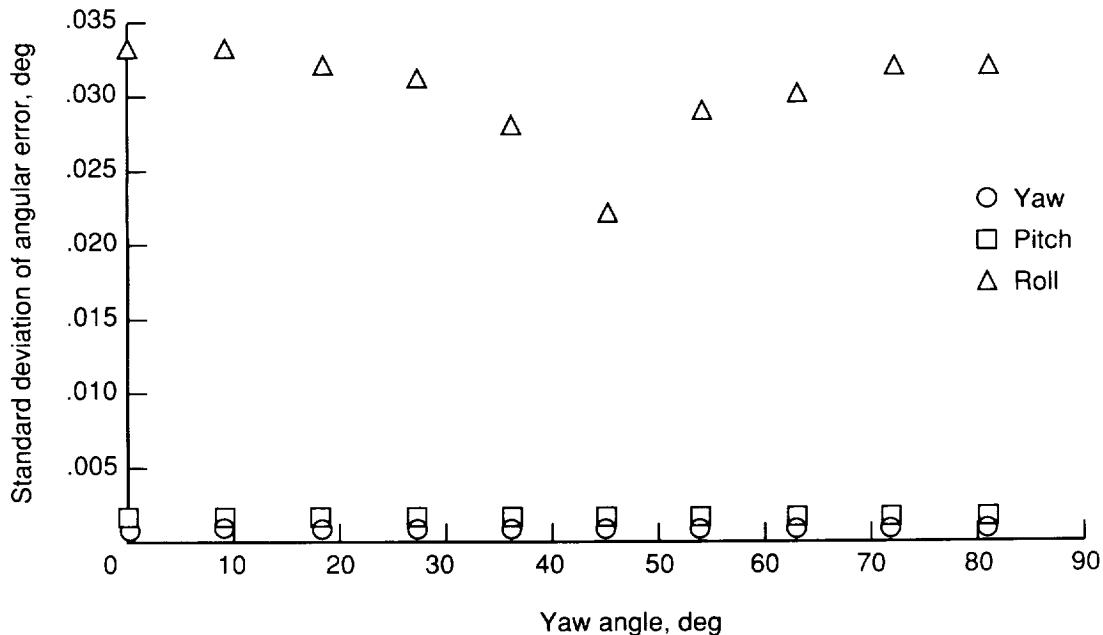
(b) Predicted error as function of yaw angle.

Figure 23. Nominal element position of x_{cm}, y_{cm}, and $z_{cm} = 0$ in.; θ and $\phi = 0°$.
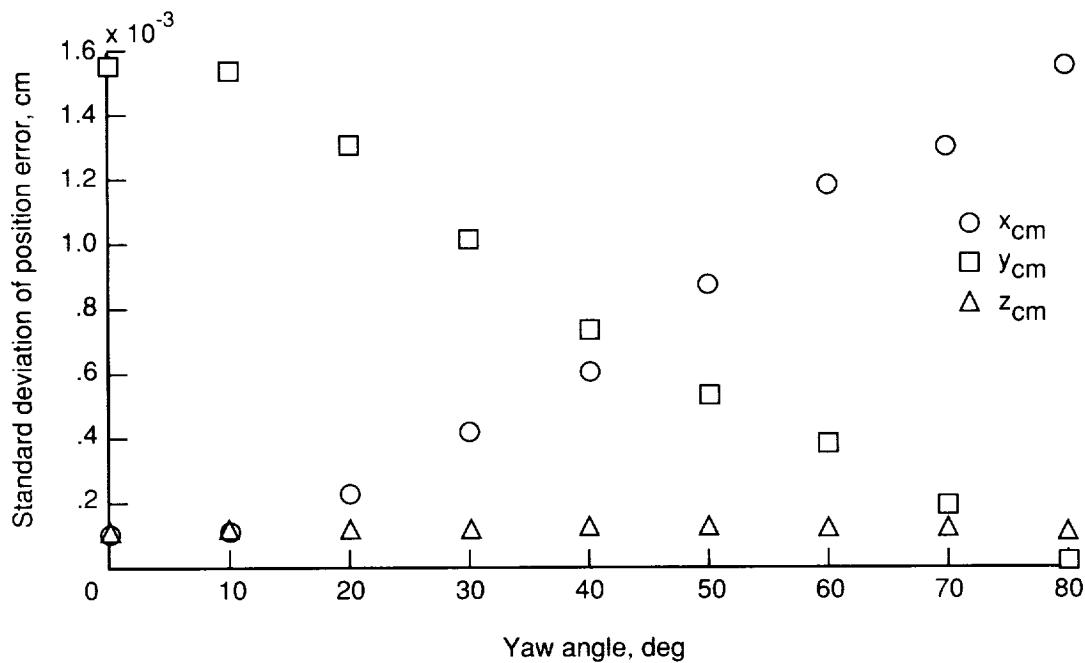
(a) Predicted error as function of yaw angle (maximum centroid accuracy assumed to be 0.03 pixel).
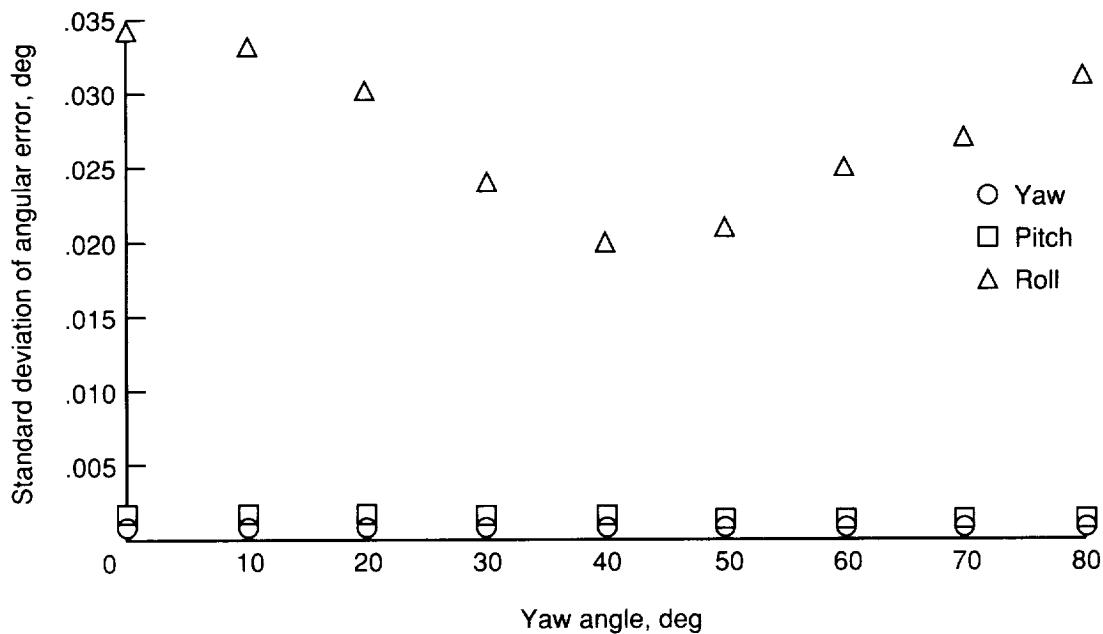
(b) Predicted error as function of yaw angle.

Figure 24. Nominal element position of x_{cm}, y_{cm}, and z_{cm} = 0 in.; θ and ϕ = 5°.
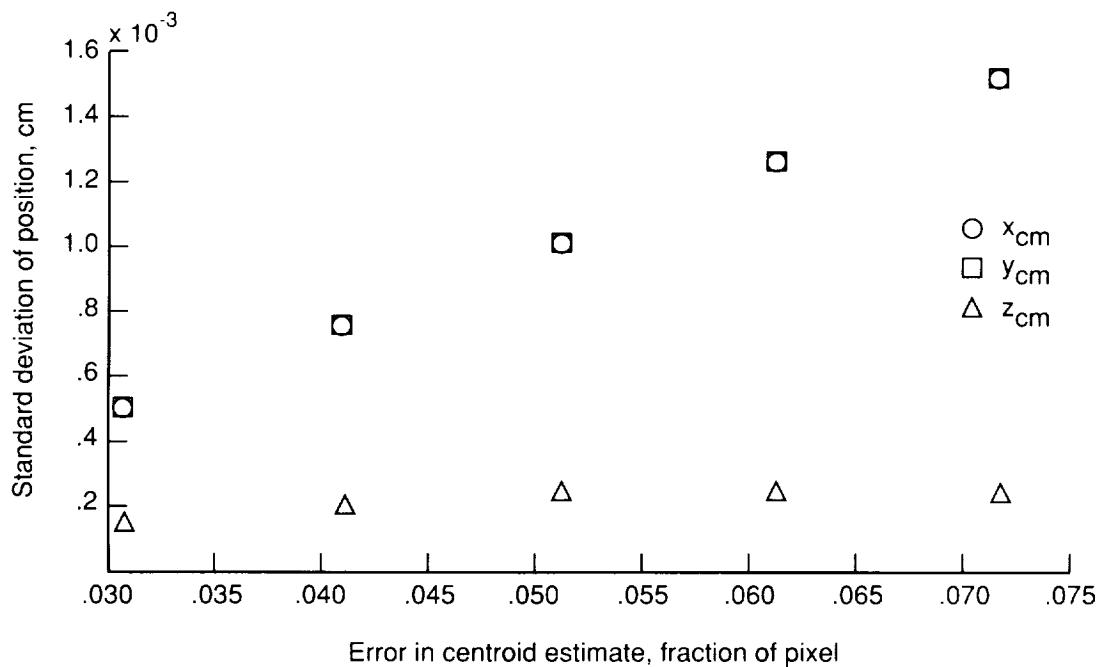
(a) Predicted error as function of standard deviation of error in centroid estimate.
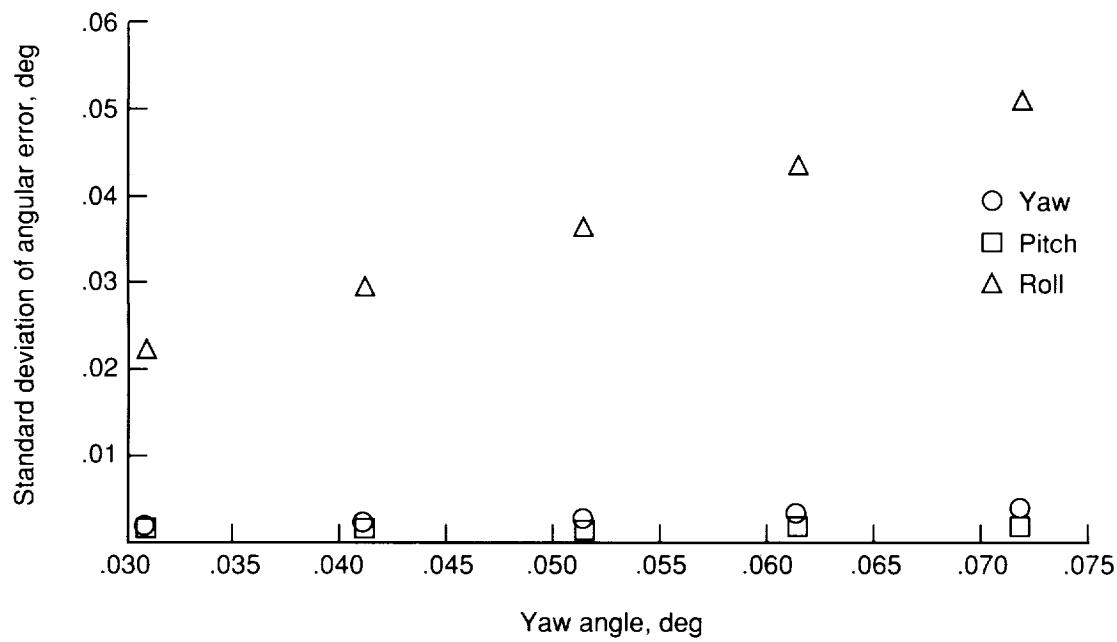
(b) Predicted error as function of standard deviation of error in centroid estimate.

Figure 25. Experiment with all cameras assumed to have same sensitivity and noise. Nominal position of element is in all degrees of freedom.
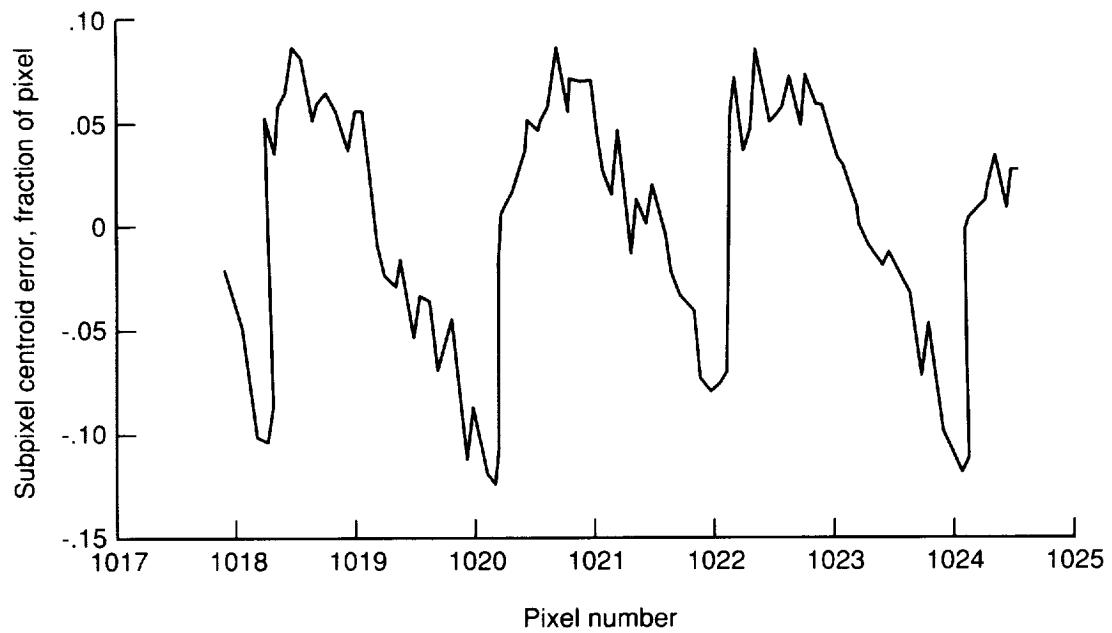
Figure 26. Systematic error in subpixel centroid estimate resulting from drift in two output voltage signals from camera. Error is periodic (every two pixels).
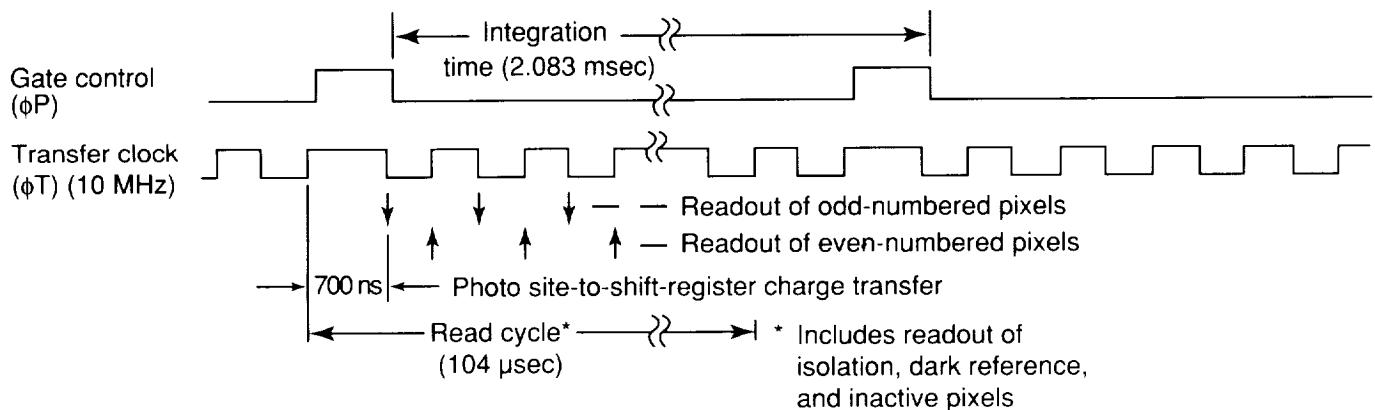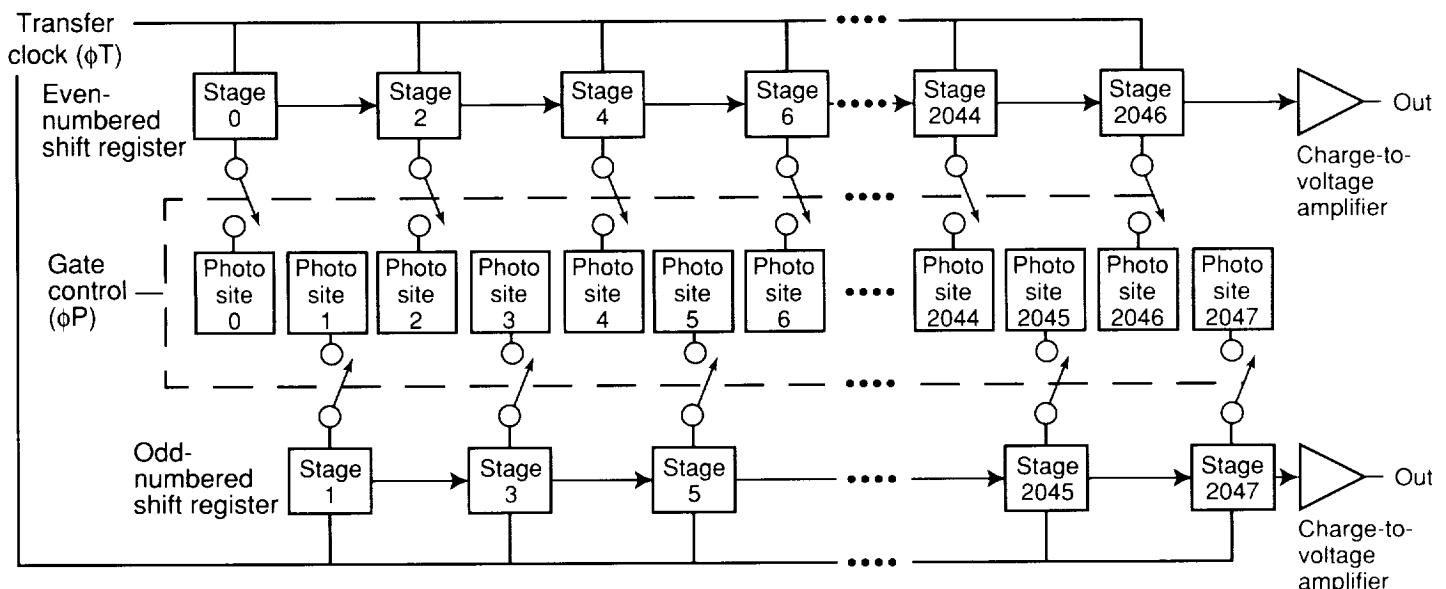
Figure 27. CCD array charge transfer circuitry and timing.
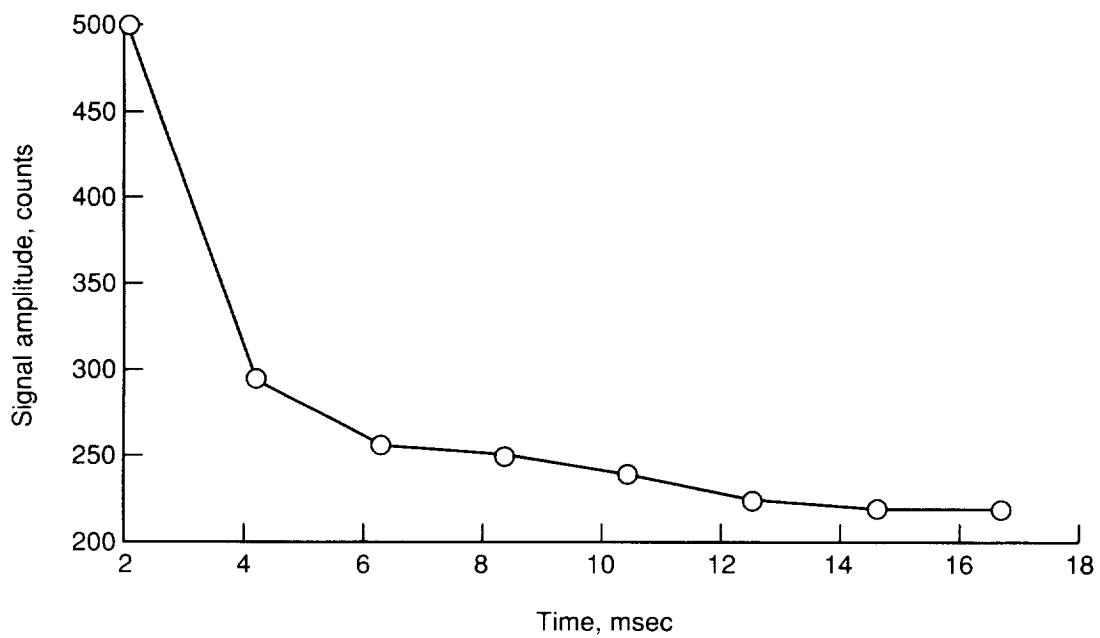
Figure 28. Peak output signal of LED target image over eight consecutive read cycles. LED target was illuminated during integration period preceding first read cycle.
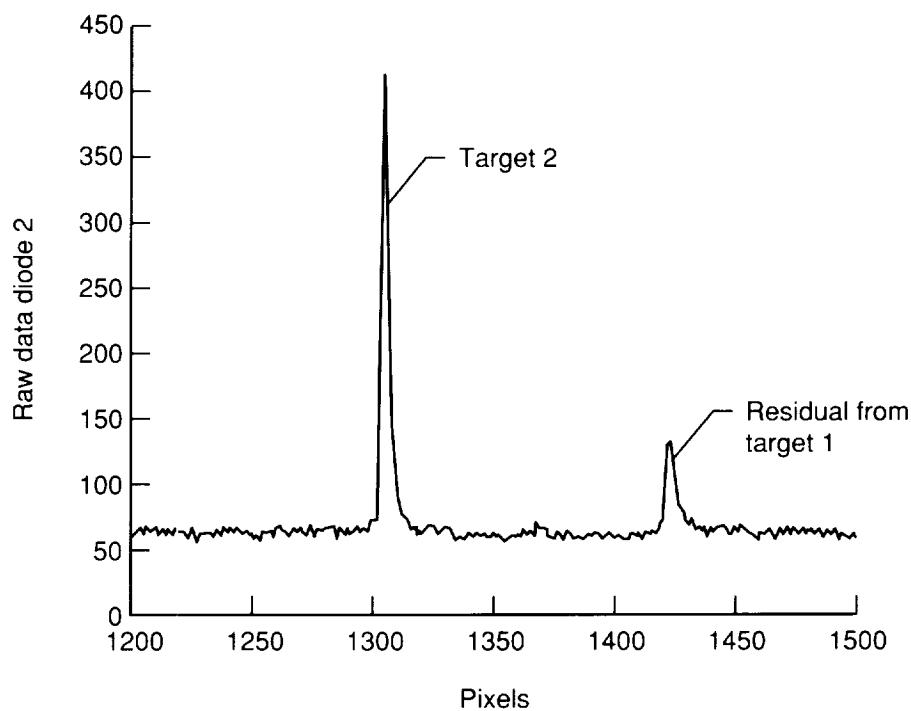
(a) Unfiltered digital signal from camera 10 for 2.083 msec integration time.
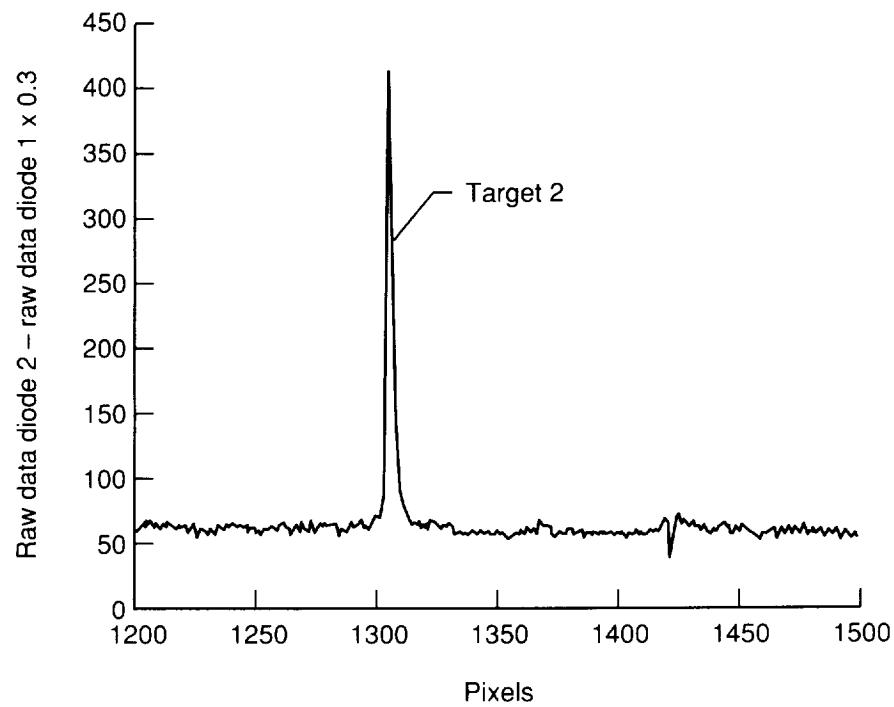
(b) Signal filtered to remove residual.

Figure 29. Images of target and residual from target 1.
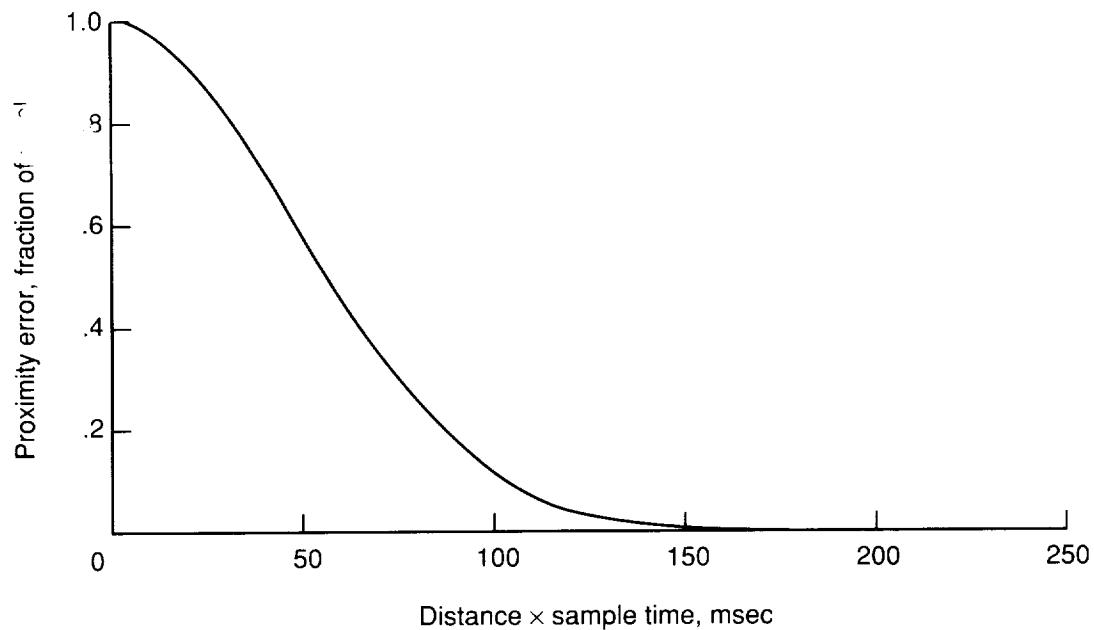
Figure 30. Empirically derived function used to estimate proximity error of current target sample as function of difference in distance between current target sample and target after image and difference in acquisition time between current sample and target after image.
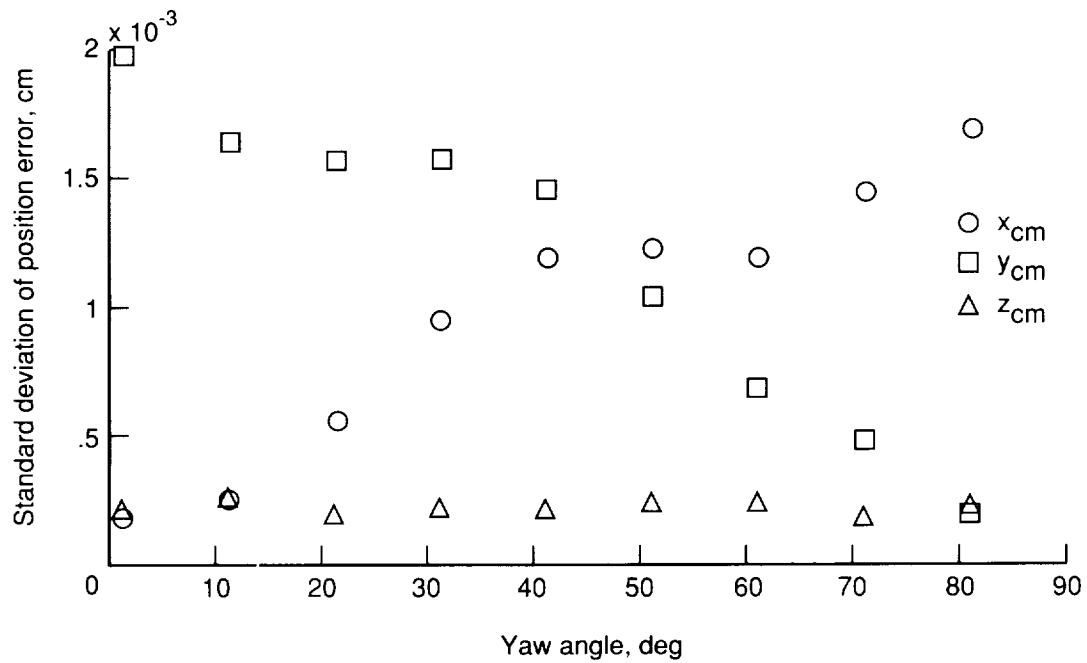
(a) Predicted error in position estimate of cylinder as function of yaw angle.
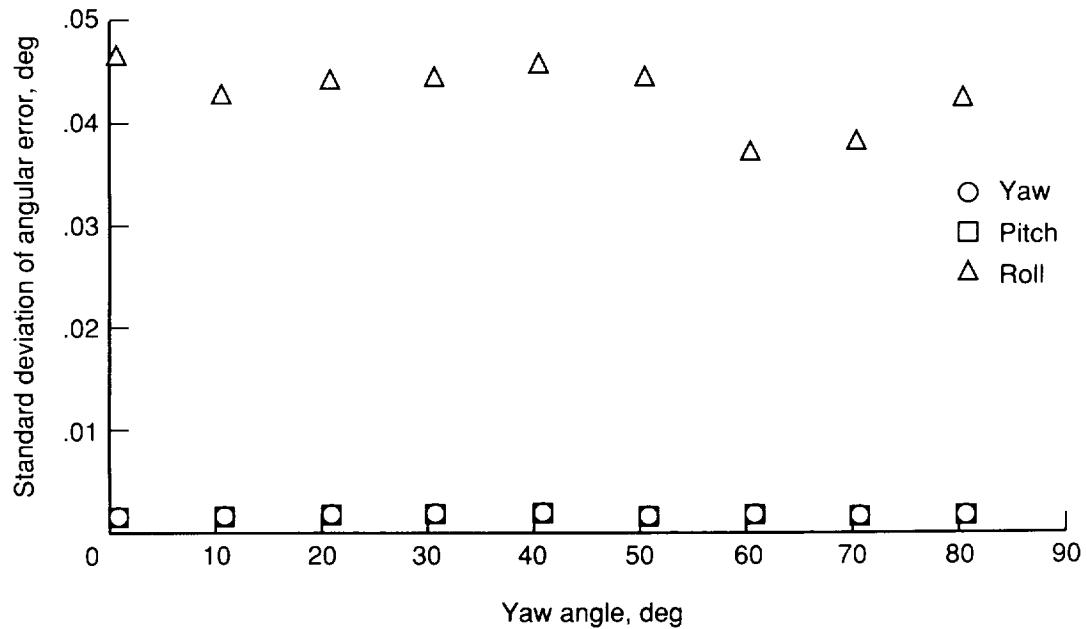
(b) Predicted error in attitude of cylinder as function of yaw angle.

Figure 31. Assumed minimum centroid error of 0.03 pixel; 0.01 pixel assumed for residual optics error; proximity error included.
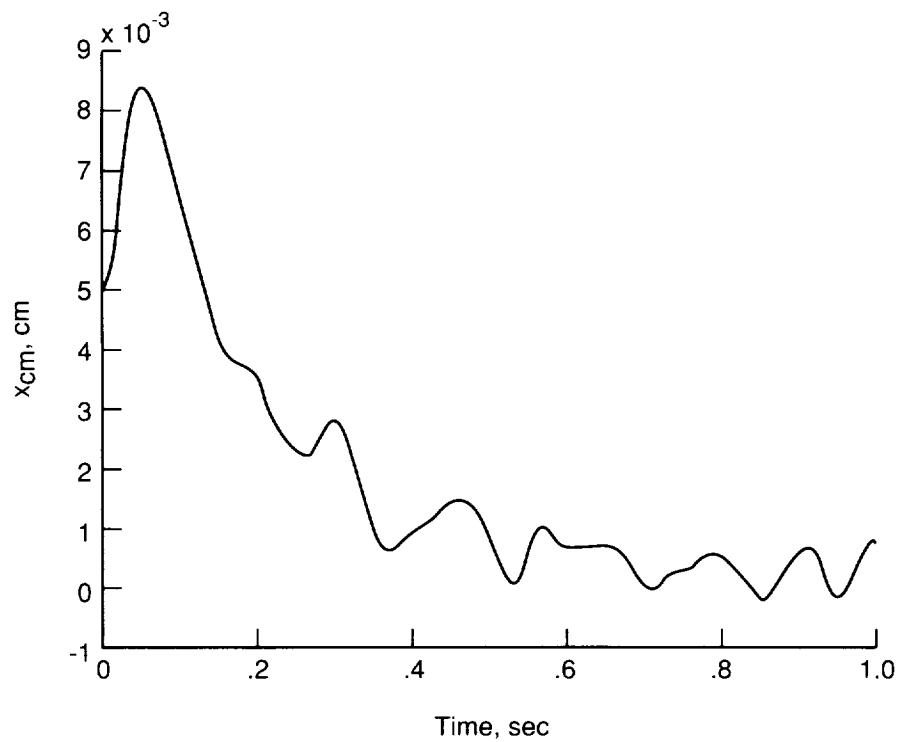
(a) Predicted x_{cm} trajectory of cylinder during launch by mechanical injection device. Element assumed displaced in x initially, then moves to origin of laboratory reference frame under influence of control system.
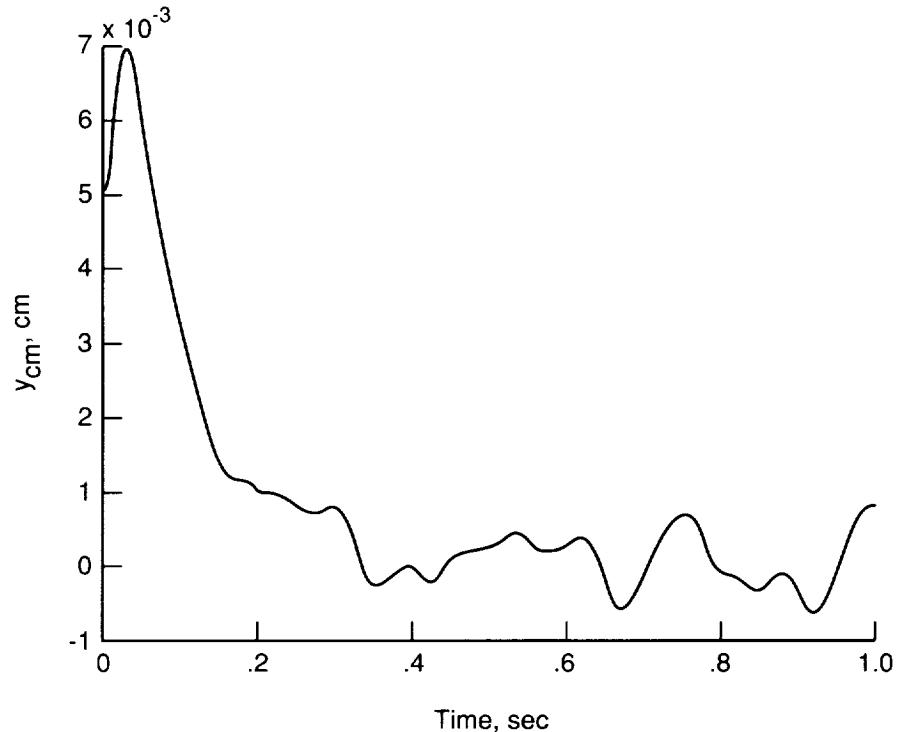
(b) Predicted y_{cm} trajectory of element during launch.

Figure 32. Input trajectory after release by injection device.
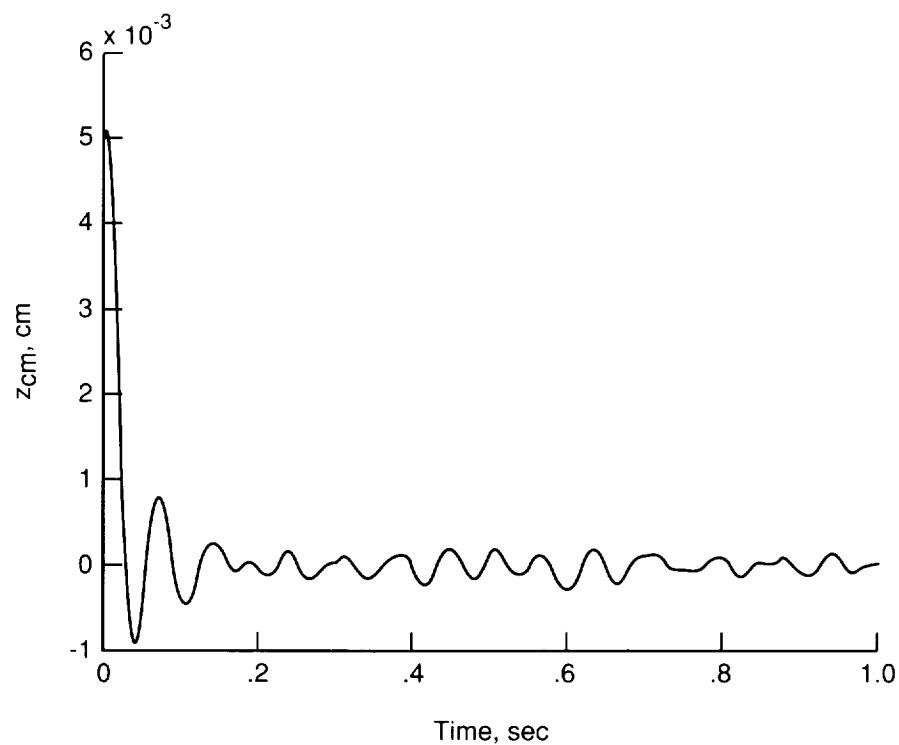
(c) Predicted z_{cm} trajectory of element during launch.
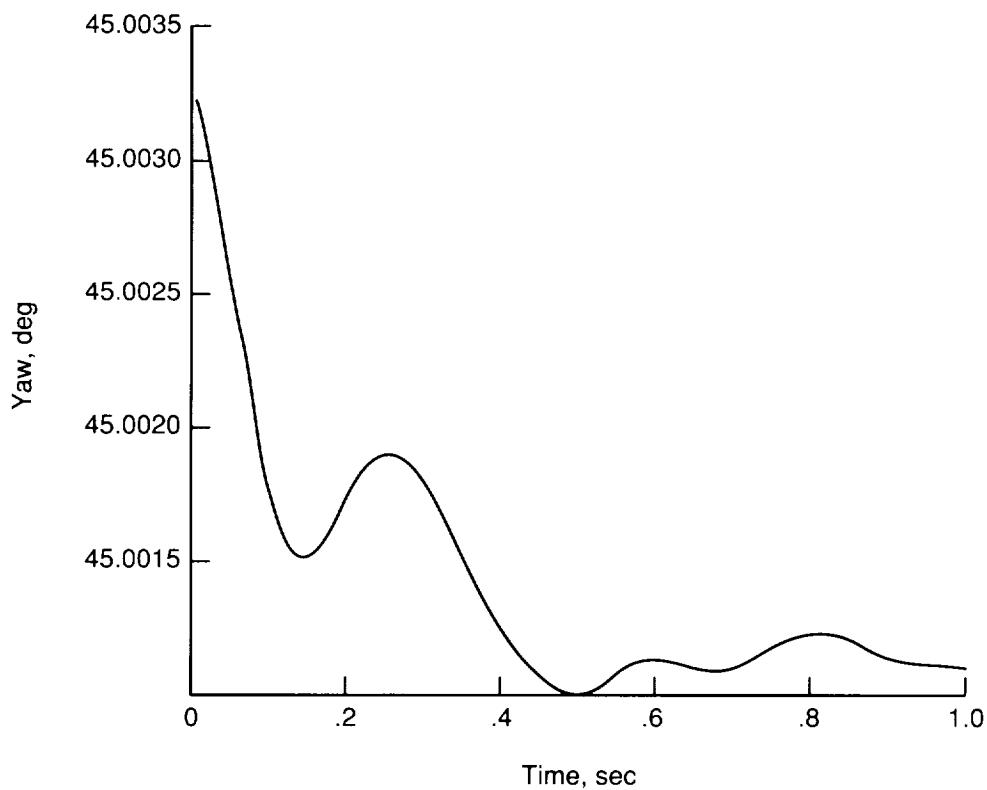
(d) Predicted yaw trajectory of element during launch.

Figure 32. Continued.
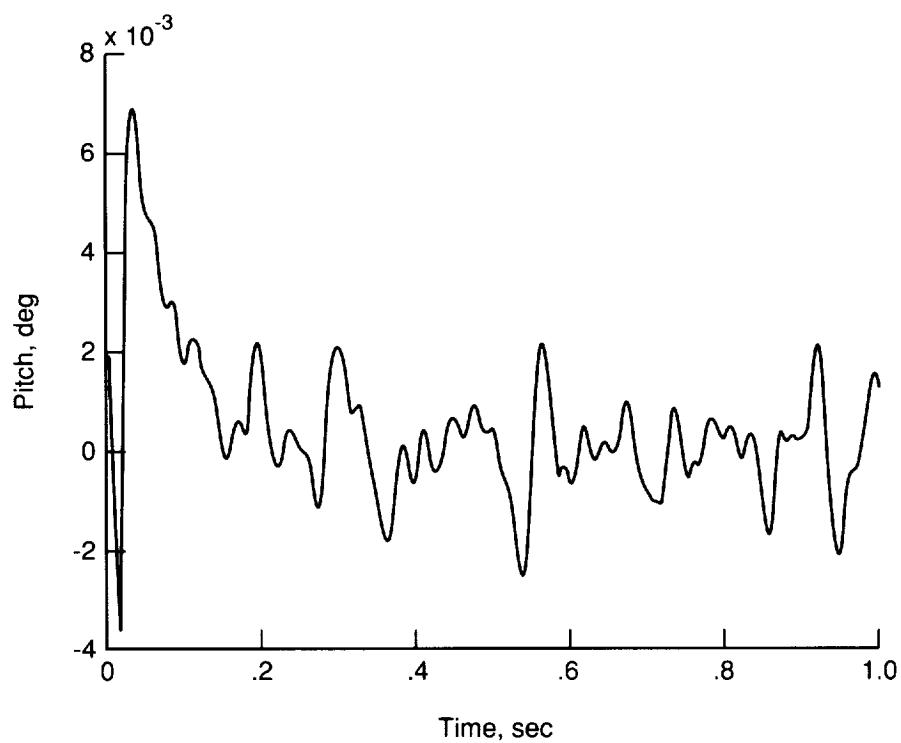
(e) Predicted pitch trajectory of element during launch.
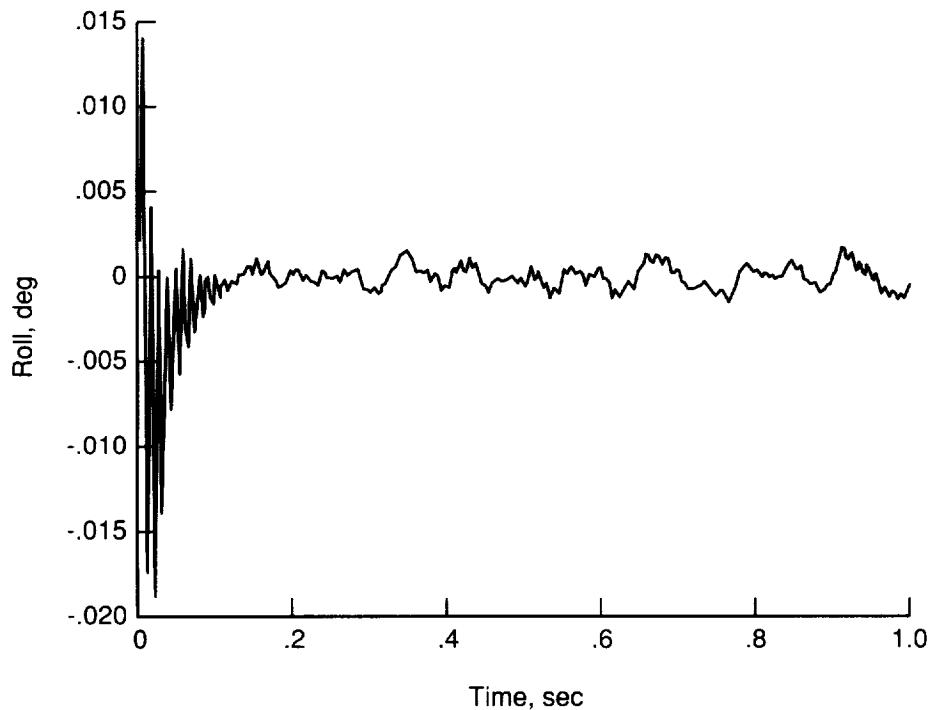
(f) Predicted roll trajectory of element during launch.

Figure 32. Concluded.

44
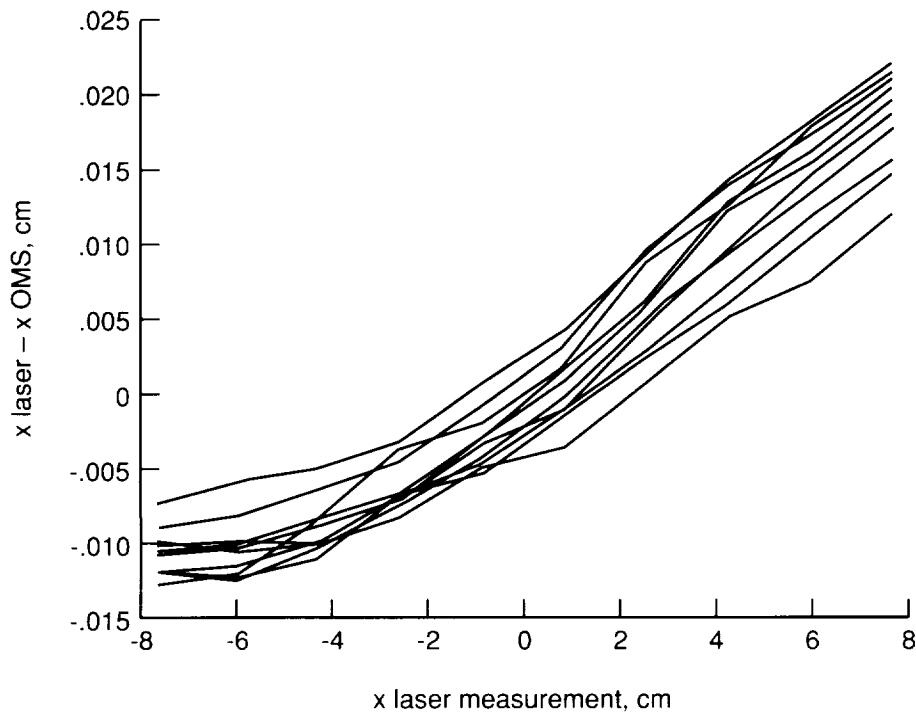
(a) Differences between x displacement measured by laser and x_f measured by OMS as function of x displacement. Different lines correspond to different values of y displacement.
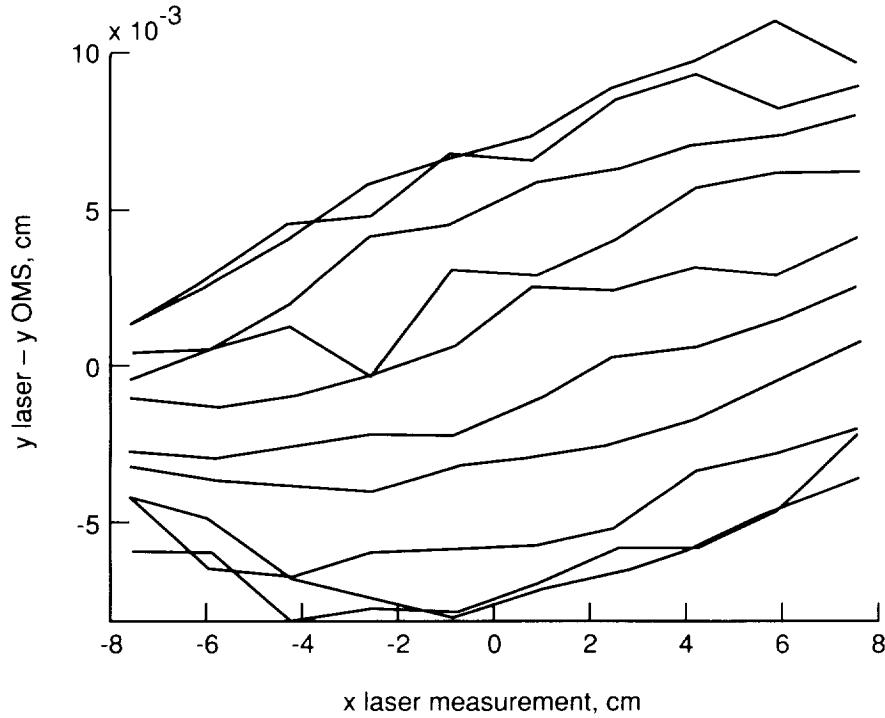
(b) Differences between y displacement measured by laser and y_f measured by OMS as function of x displacement. Different lines correspond to different values of y displacement.

Figure 33. OMS-predicted LED coordinates versus laser predictions.

45
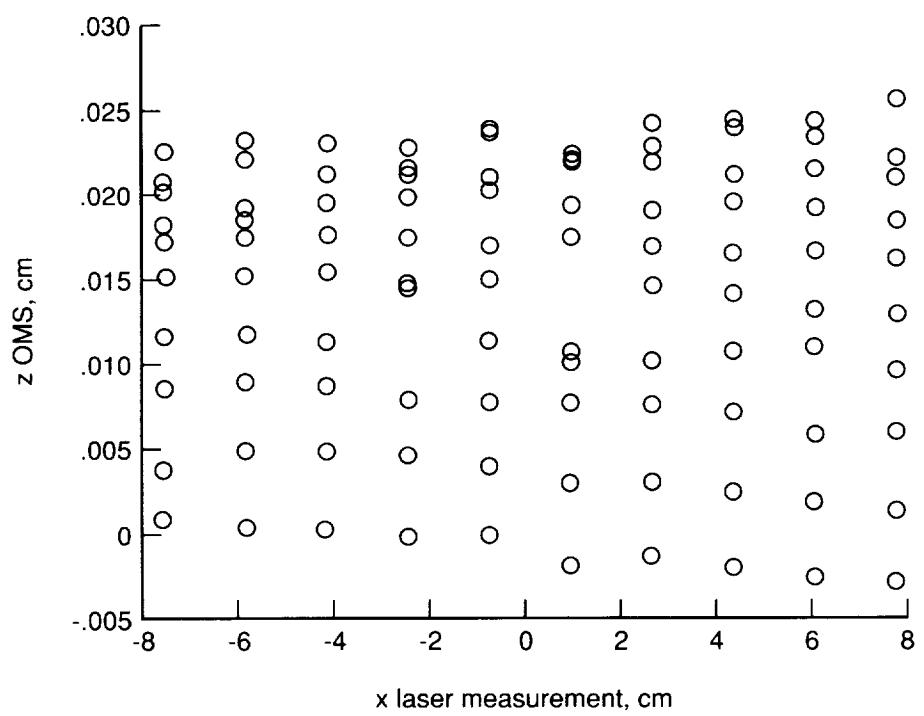
(c) z_f measured by OMS as function of x displacement.

Figure 33. Concluded.
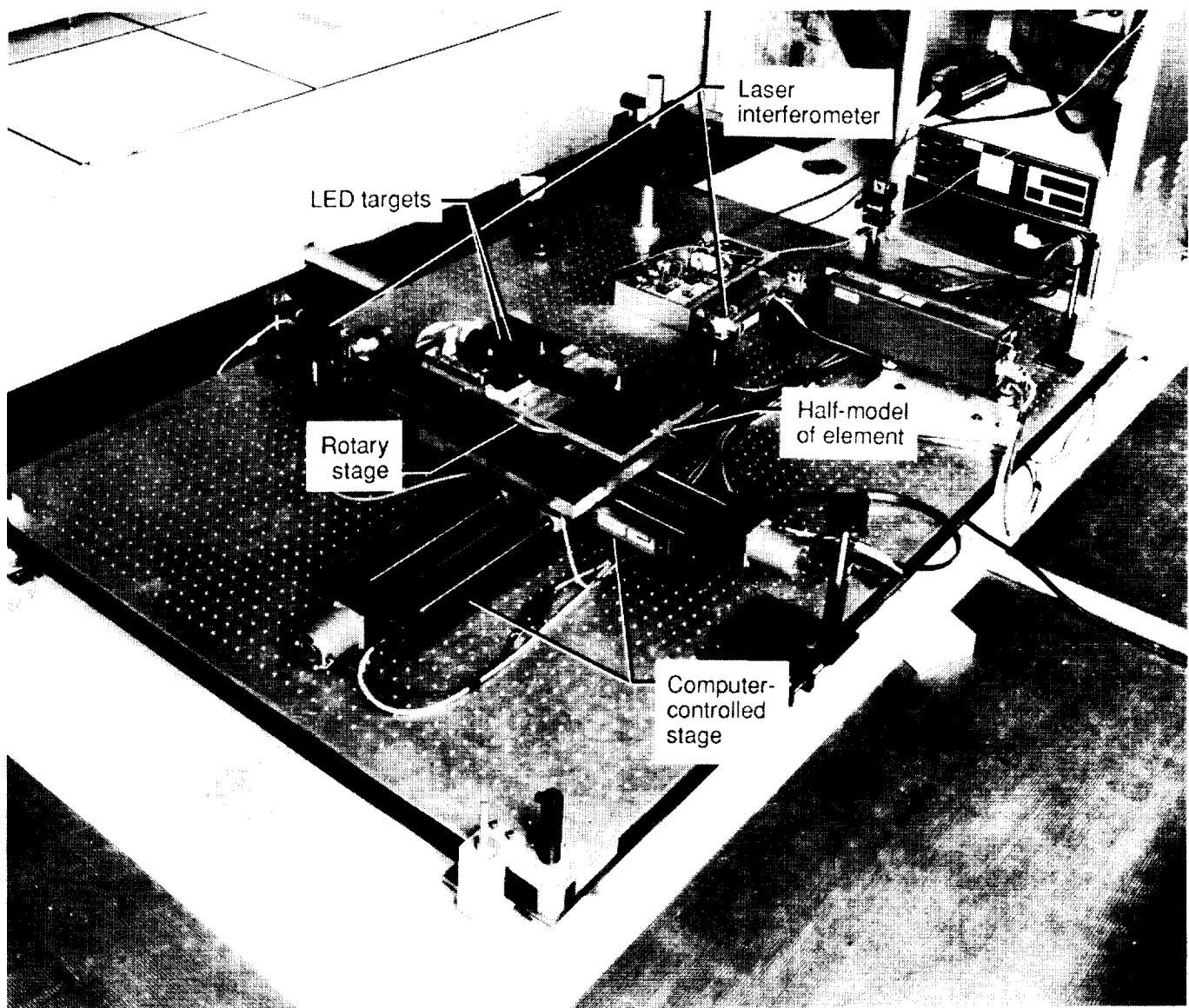
L-92-10961

Figure 34. Experimental setup for measuring position and attitude of suspended element using element half-model.
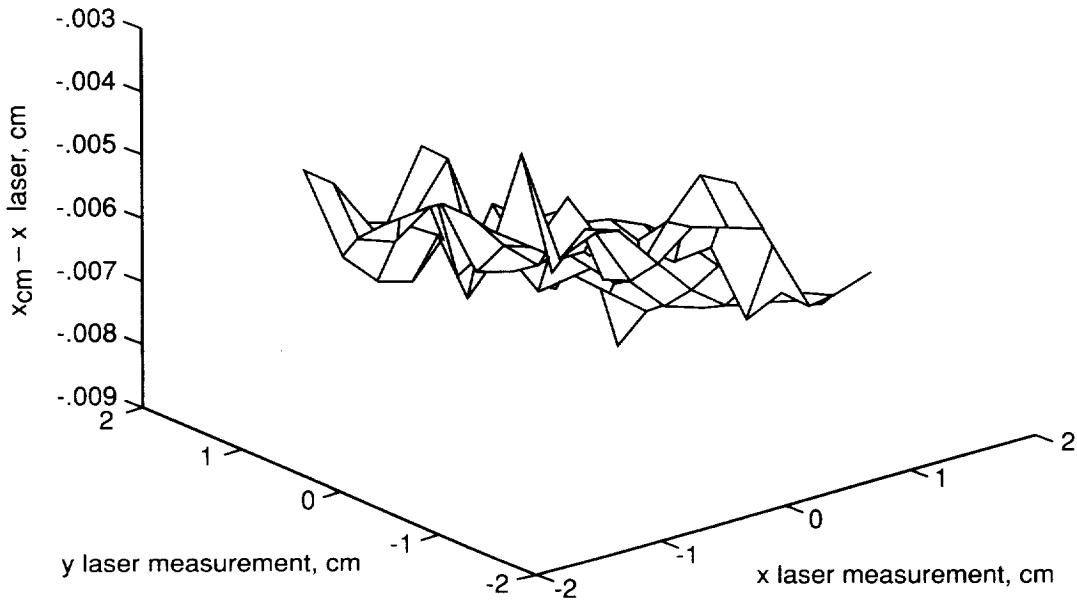
(a) Difference between average x_{cm} measurement from OMS and average laser measurement over ±1.25-cm displacement in x and y for 10 by 10 grid.
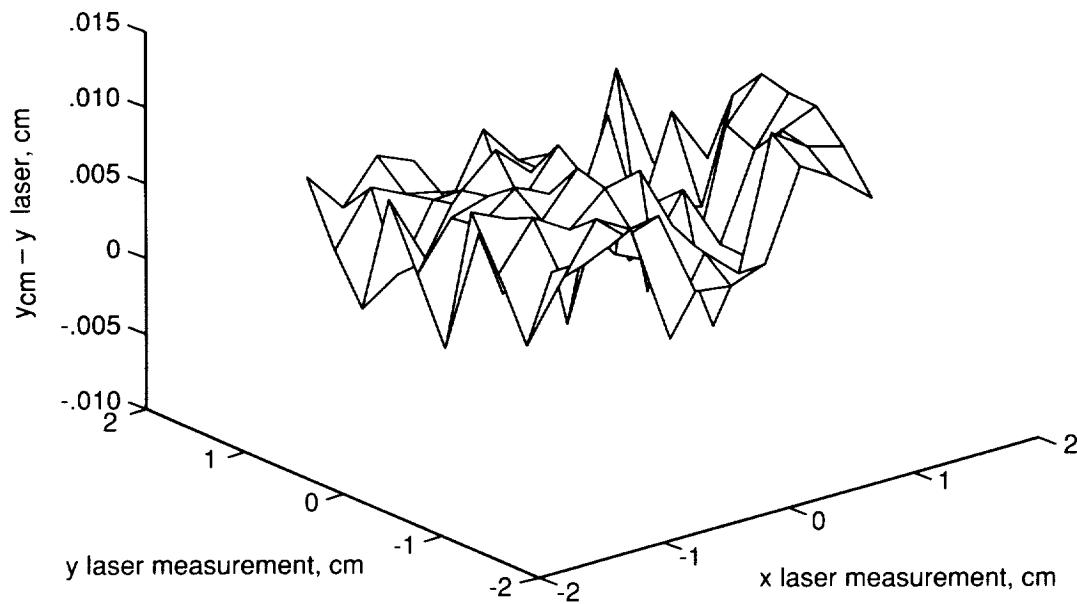

(b) Difference between average y_{cm} measurement from OMS and average laser measurement over ±1.25-cm displacement in x and y for 10 by 10 grid.

Figure 35. Three-dimensional plot of half-model experiment.
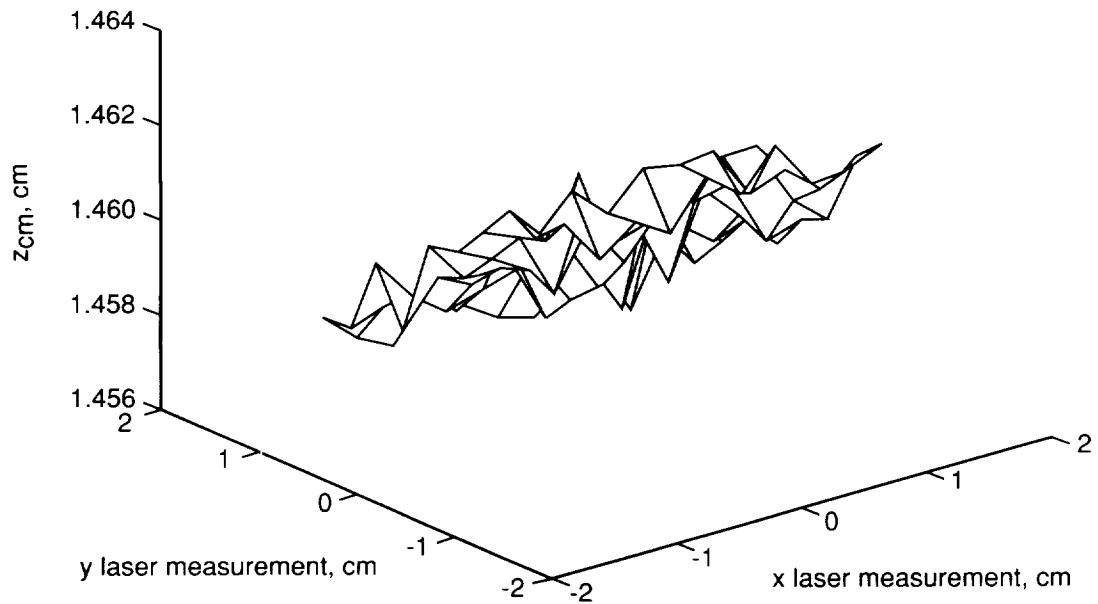
(c) Average z_{cm} measurement from OMS over ± 1.25-cm displacement in x and y for 10 by 10 grid.
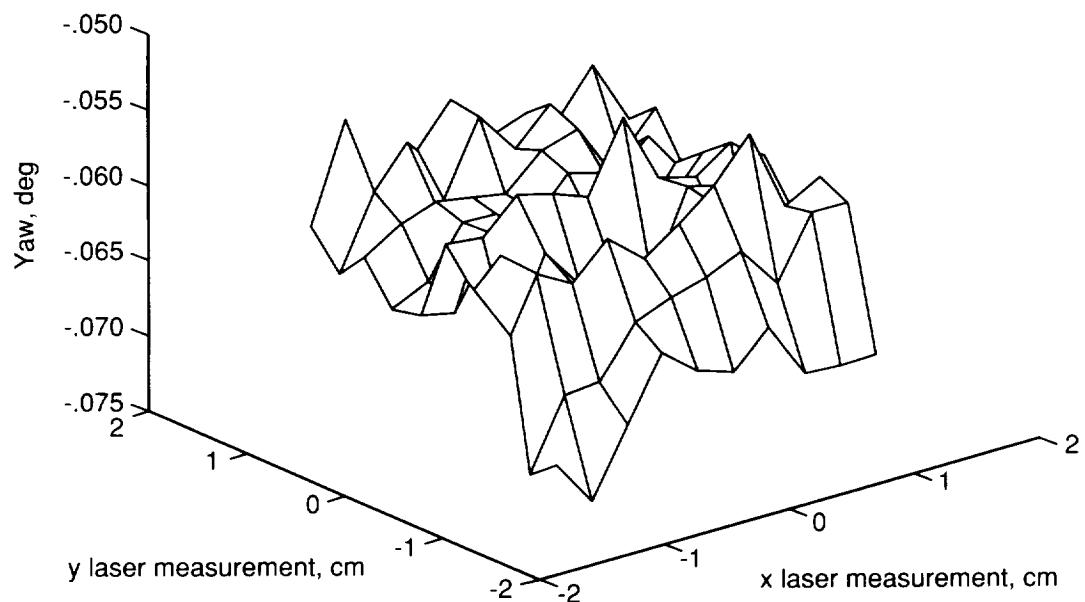
(d) Average yaw measurement from OMS over ± 1.25-cm displacement in x and y for 10 by 10 grid.

Figure 35. Continued.
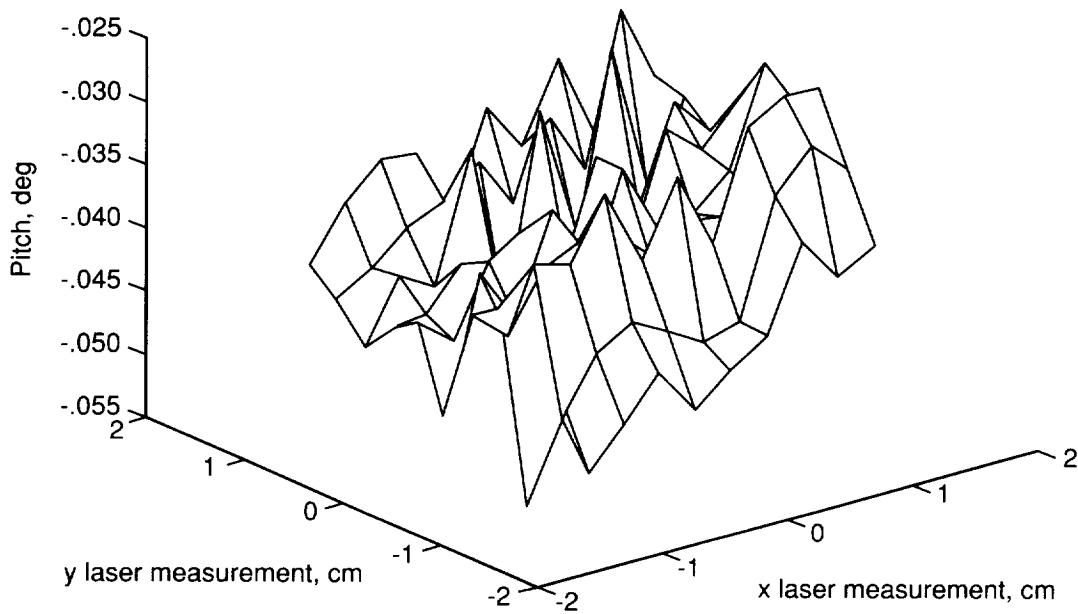
(e) Average pitch measurement from OMS over ±1.25-cm displacement in x and y for 10 by 10 grid.
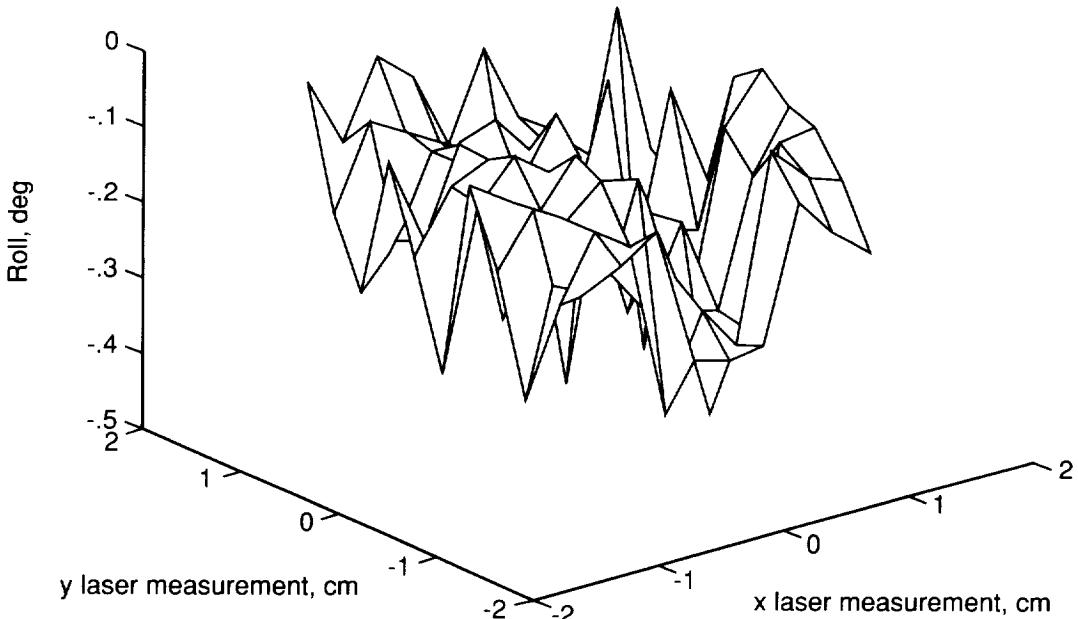

(f) Average roll measurement from OMS over ±1.25-cm displacement in x and y for 10 by 10 grid.

Figure 35. Concluded.

50
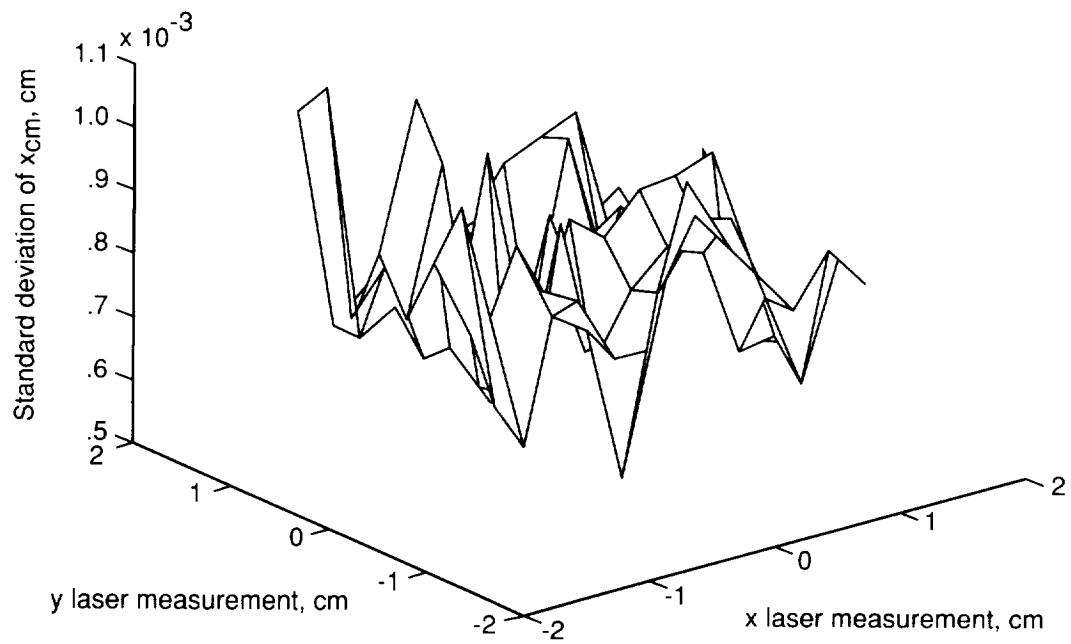
(a) Standard deviation of x_{cm} measurement from OMS over ± 1.25-cm displacement in x and y for 10 by 10 grid.
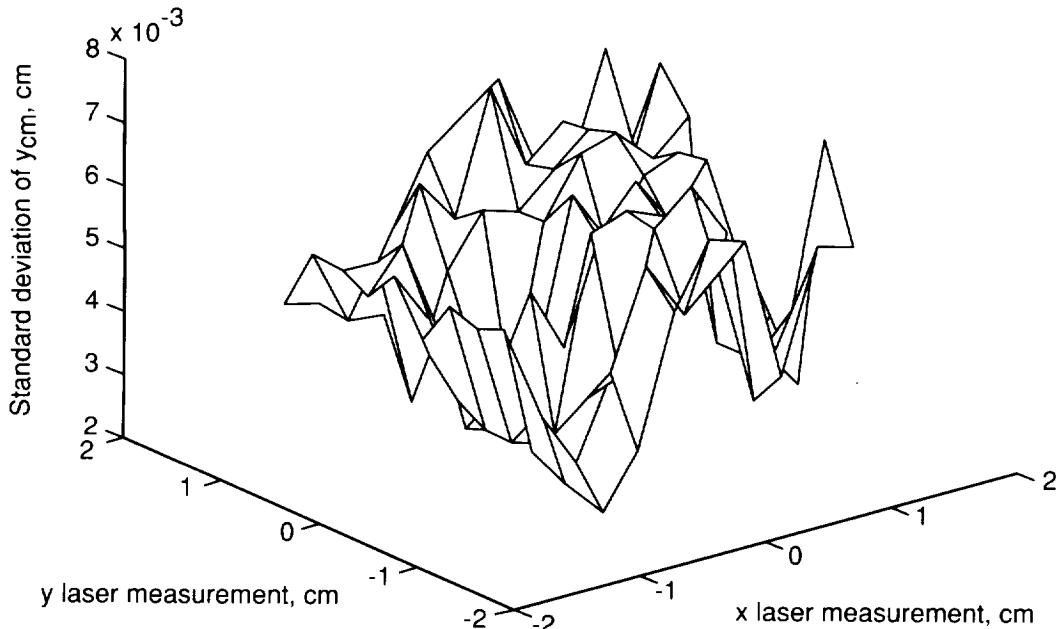

(b) Standard deviation of y_{cm} measurement from OMS over ± 1.25-cm displacement in x and y for 10 by 10 grid.

Figure 36. Three-dimensional plots showing standard deviations for half-model experiment.
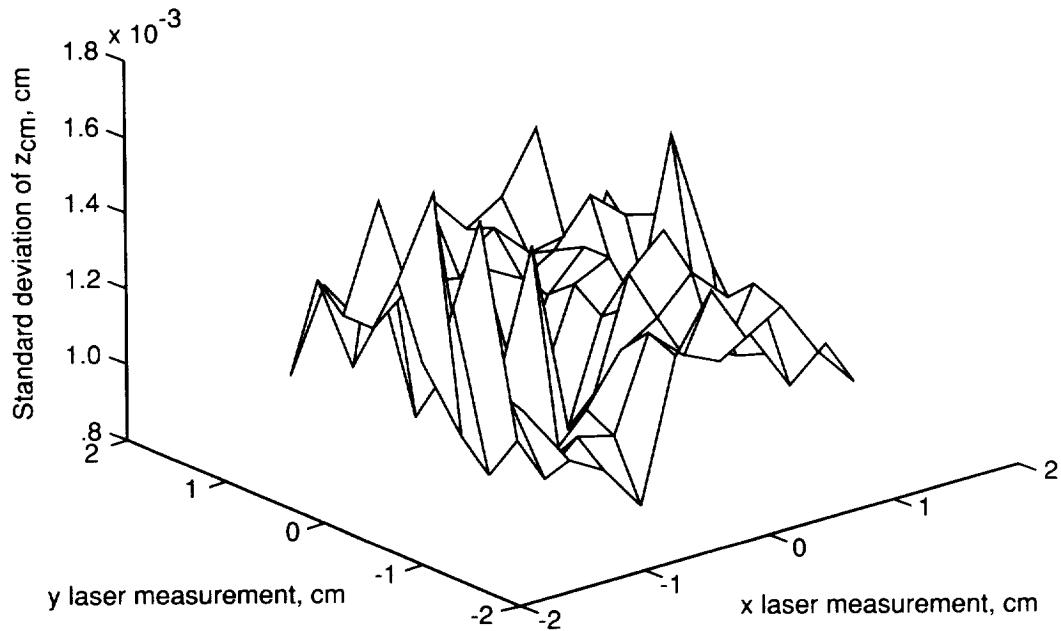
(c) Standard deviation of z_{cm} measurement from OMS over ±1.25-cm displacement in x and y for 10 by 10 grid.
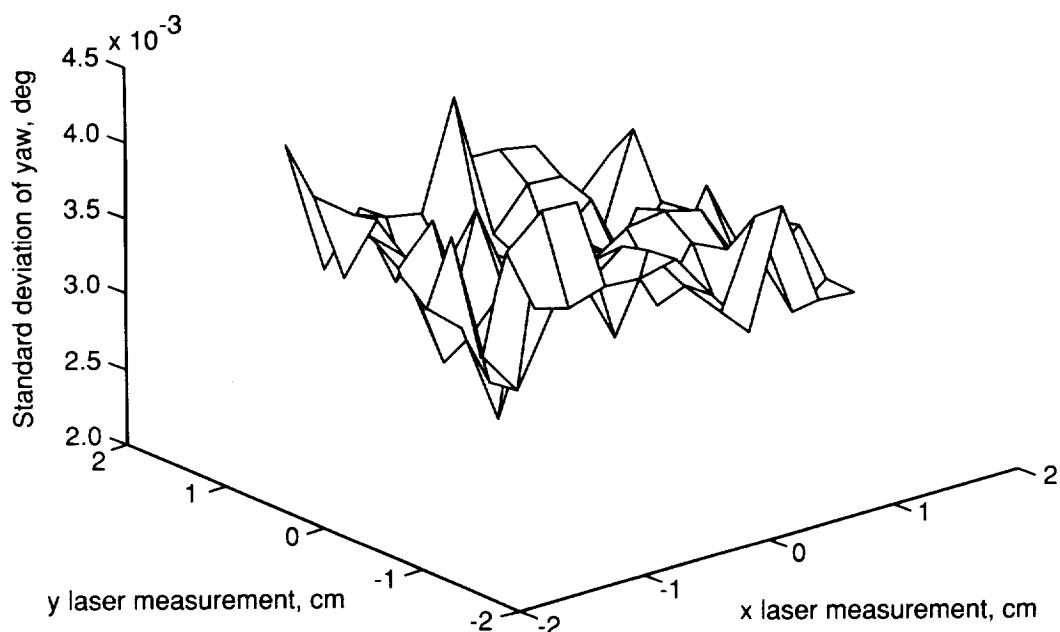

(d) Standard deviation of yaw measurement from OMS over ±1.25-cm displacement in x and y for 10 by 10 grid.

Figure 36. Continued.
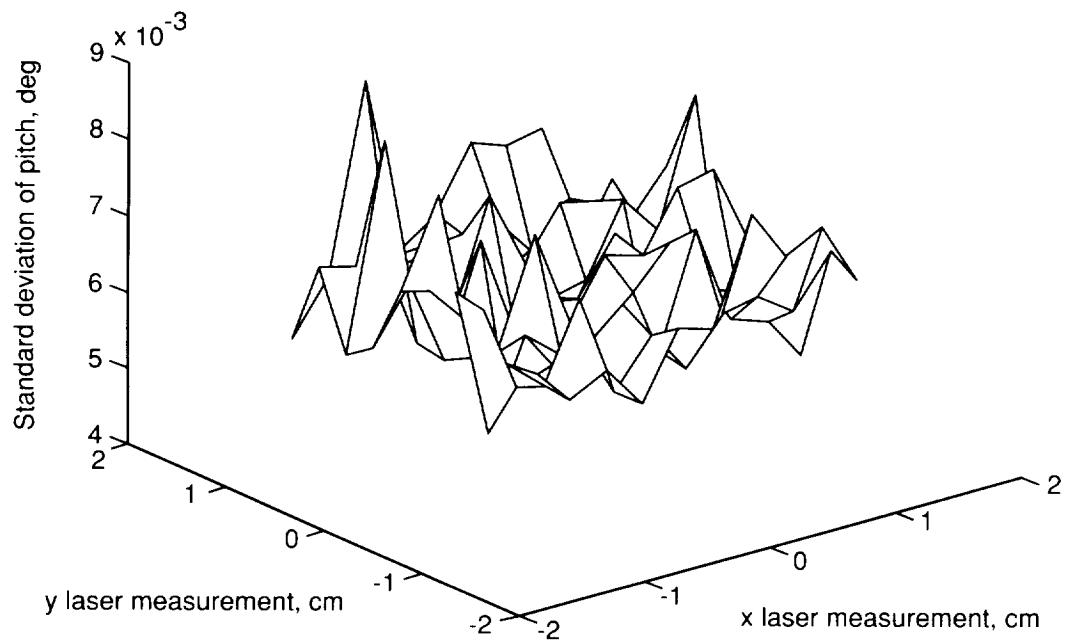
(e) Standard deviation of pitch measurement from OMS over ±1.25-cm displacement in x and y for 10 by 10 grid.
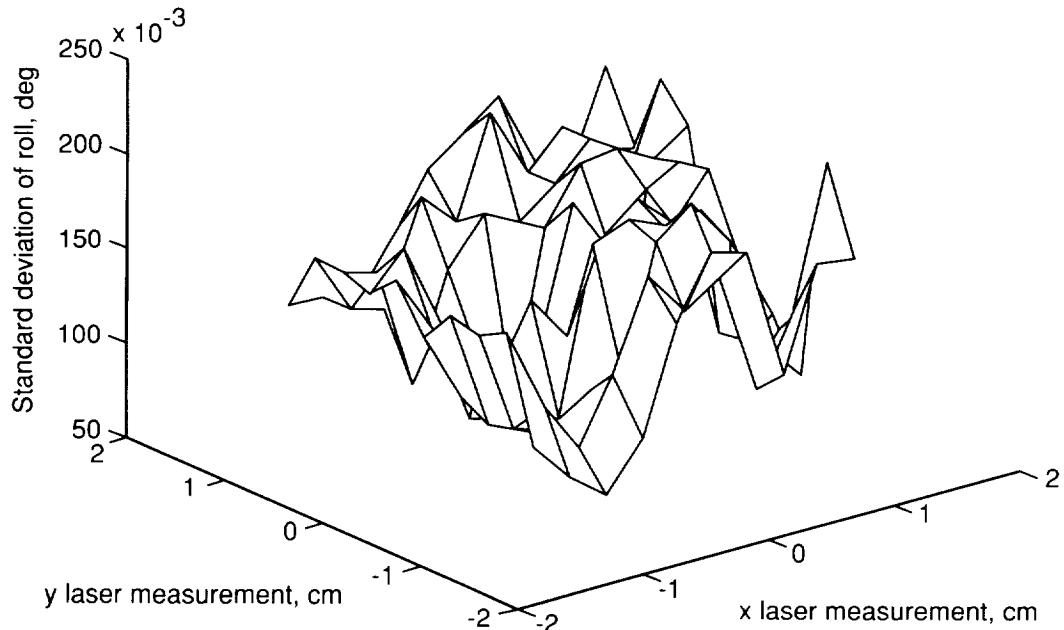
(f) Standard deviation of roll measurement from OMS over ±1.25-cm displacement in x and y for 10 by 10 grid.

Figure 36. Concluded.

REPORT DOCUMENTATION PAGE

Public reporting burden for this collection of information is estimated to average 1 hour per response, including the time for reviewing instructions, searching existing data sources, gathering and maintaining the data needed, and completing and reviewing the collection of information. Send comments regarding this burden estimate or any other aspect of this collection of information, including suggestions for reducing this burden, to Washington Headquarters Services, Directorate for Information Operations and Reports, 1215 Jefferson Davis Highway, Suite 1204, Arlington, VA 22202-4302, and to the Office of Management and Budget, Paperwork Reduction Project (0704-0188), Washington, DC 20503

1. AGENCY USE ONLY(Leave blank)	2. REPORT DATE	3. REPORT TYPE AND DATES COVERED
	June 1994	Technical Paper

4. TITLE AND SUBTITLE
Optical Position Measurement for a Large Gap Magnetic Suspension System
Design and Performance Analysis

5. FUNDING NUMBERS
WU 506-59-61-04

6. AUTHOR(S)
Sharon S. Welch, James I. Clemmons, Jr., Kevin J. Shelton, and Walter C. Duncan

7. PERFORMING ORGANIZATION NAME(S) AND ADDRESS(ES)
NASA Langley Research Center
Hampton, VA 23681-0001

8. PERFORMING ORGANIZATION REPORT NUMBER
L-17257

9. SPONSORING/MONITORING AGENCY NAME(S) AND ADDRESS(ES)
National Aeronautics and Space Administration
Washington, DC 20546-0001

10. SPONSORING/MONITORING AGENCY REPORT NUMBER
NASA TP-3438

11. SUPPLEMENTARY NOTES
Welch: Langley Research Center, Hampton, VA; Clemmons: ViGYAN, Inc., Hampton, VA; Shelton and Duncan: Lockheed Engineering & Sciences Company, Hampton, VA.

12a. DISTRIBUTION/AVAILABILITY STATEMENT

Unclassified Unlimited

Subject Category 36

12b. DISTRIBUTION CODE

13. ABSTRACT (Maximum 200 words)
An optical measurement system (OMS) has been designed and tested for a large gap magnetic suspension system (LGMSS). The LGMSS will be used to study control laws for magnetic suspension systems for vibration isolation and pointing applications. The LGMSS features six degrees of freedom and consists of a planar array of electromagnets that levitate and position a cylindrical element containing a permanent magnet core. The OMS provides information on the location and orientation of the element to the LGMSS control system to stabilize suspension. The hardware design of this optical sensing system and the tracking algorithms are presented. The results of analyses and experiments are presented that define the accuracy limits of the optical sensing system and that quantify the errors in position estimation.

14. SUBJECT TERMS
Optical position measurement; Point tracking; Centroiding

15. NUMBER OF PAGES
54

16. PRICE CODE
A04

17. SECURITY CLASSIFICATION OF REPORT	18. SECURITY CLASSIFICATION OF THIS PAGE	19. SECURITY CLASSIFICATION OF ABSTRACT	20. LIMITATION OF ABSTRACT
Unclassified	Unclassified		

National Aeronautics and
Space Administration
Langley Research Center
Mail Code 180
Hampton, VA 23681-00001

Official Business
Penalty for Private Use, $300